

Neutral Hydrogen in the Ringed Barred Galaxies NGC 1433 and
NGC 6300

Ronald J. Buta – University of Alabama
et al.

Deposited 06/11/2019

Citation of published version:

Ryder, S., et al. (1996): Neutral Hydrogen in the Ringed Barred Galaxies NGC 1433 and NGC 6300. *The Astrophysical Journal*, vol. 460.

DOI: [10.1086/177000](https://doi.org/10.1086/177000)

NEUTRAL HYDROGEN IN THE RINGED BARRED GALAXIES NGC 1433 AND NGC 6300¹

STUART D. RYDER,² RONALD J. BUTA, HECTOR TOLEDO,³ AND HEMANT SHUKLA
 Department of Physics and Astronomy, University of Alabama, Box 870324, Tuscaloosa, AL 35487-0324;
 sdr@newt.phys.unsw.edu.au, buta@sarah.astr.ua.edu

LISTER STAVELEY-SMITH
 Australia Telescope National Facility, CSIRO, P.O. Box 76, Epping, NSW 2121, Australia; lstavele@atnf.csiro.au

AND

WILFRED WALSH
 School of Physics, University of New South Wales, Sydney 2052, Australia; and Australia Telescope National Facility,
 CSIRO, P.O. Box 76, Epping, NSW 2121, Australia; wwalsh@atnf.csiro.au

Received 1995 July 13; accepted 1995 October 3

ABSTRACT

We have made observations of the H I in the southern ringed barred spiral galaxies NGC 1433 and NGC 6300 with the Australia Telescope Compact Array (ATCA), the main goal being to test the resonance theory for the origin of these rings. NGC 1433 is the prototypical ringed barred spiral and displays distinct H I counterparts to its nuclear ring, inner ring, outer pseudoring, and plumelike features. The L_4 and L_5 regions at corotation, as well as the bar itself, are relatively devoid of neutral atomic hydrogen. We use the Tully-Fisher relation to argue that the mean inclination of the disk of NGC 1433 is closer to 33° than to 20° , meaning that its outer pseudoring is intrinsically almost circular, while the inner ring is rather more elongated than the average (based on results from the Catalog of Southern Ringed Galaxies). Strong radio continuum emission is localized to the nucleus and the ends of the bar in NGC 1433, and we place an upper limit on the 1.38 GHz flux of the Type II SN 1985P a decade after the explosion. By associating the inner ring of NGC 1433 with the inner second harmonic resonance, and its outer pseudoring with the outer Lindblad resonance, we are able to infer a bar pattern speed for NGC 1433 of $26 \pm 5 \text{ km s}^{-1} \text{ kpc}^{-1}$.

By way of contrast, NGC 6300 possesses a much more extended H I disk than NGC 1433, despite having a similar morphological type. There is a gas ring underlying the inner pseudoring, but it is both broader and slightly larger in diameter than the optical feature. The outer H I envelope has a 20° kinematic warp as well as a short tail, even though there are no nearby candidates for a recent interaction with NGC 6300. The noncircular motions inferred from optical emission-line spectra do not appear to extend beyond the bar region of NGC 6300. Barely 10% of the 1.38 GHz radio continuum emission in NGC 6300 originates in the type 2 Seyfert nucleus, with the rest coming from a disklike component internal to the ring. By again linking an inner ring feature to the inner second harmonic resonance, we derive a bar pattern speed for NGC 6300 of $27 \pm 8 \text{ km s}^{-1} \text{ kpc}^{-1}$, but in this case, neither the outer pseudoring nor the nuclear ring predicted by the resonance ring theory can be identified in NGC 6300. Although it may be the case that the ring in NGC 6300 is not related to a resonance with the bar at all, we postulate instead that NGC 6300 is merely a less well developed example of a resonance ring galaxy than is NGC 1433.

Subject headings: galaxies: individual (NGC 1433, NGC 6300) — galaxies: kinematics and dynamics — galaxies: spiral — galaxies: structure — radio lines: galaxies

1. INTRODUCTION

The barred (SB) and weakly barred (SAB) systems comprise about two-thirds of the disk galaxy population (de Vaucouleurs 1963). Hydrodynamical models have demonstrated that even a mild oval distortion in the stellar mass distribution can generate spiral structure in the gas, leading to shocks, significant noncircular motions (up to 100 km s^{-1} in the bar region), and secular redistribution of the disk material, effects which should be especially pronounced if the bar is strong (Sellwood & Wilkinson 1993, and references therein). Furthermore, the interaction between a bar in the mass distribution and its principal resonances in the

disk can lead to distinctive concentrations of gas into ring-like structures, whose shapes and orientations with respect to the bar depend on the characteristics of the main periodic orbits in the resonance regions (Schwarz 1981).

Optical observations to date of the nuclear, inner, and outer rings and pseudorings occasionally observed in barred galaxies have strongly suggested that these features are almost certainly manifestations of three principal orbital resonances in the disk; the inner Lindblad resonance (ILR), inner second harmonic resonance (2HR⁻), and outer Lindblad resonance (OLR), respectively (Athanasoula et al. 1982; Kormendy 1982; Buta 1984, 1986a, b). These resonances occur where the bar pattern speed, Ω_p , is equal to $\Omega - \kappa/2$, $\Omega - \kappa/4$, and $\Omega + \kappa/2$, respectively (where Ω is the mean angular frequency, and κ is the radial epicyclic frequency). If these identifications are correct, then the rings can, in principle, tell us the locations of the main bar resonances and, in conjunction with the disk kinematics, allow

¹ Based on observations made with the Australia Telescope Compact Array, which is operated by CSIRO Australia Telescope National Facility.

² Current address: School of Physics, University of New South Wales, Sydney 2052, Australia.

³ Also at Instituto de Astronomía-UNAM, México.

us to directly measure the bar pattern speed, a fundamental unknown of galactic dynamics.

Furthermore, when the bar forcing (actually, a torque) exceeds some critical value ($\sim 20\%$ of the mean axisymmetric force), then orbits near the Lagrangian points, L_4 and L_5 at the corotation radius (CR, where $\Omega = \Omega_p$), will be swept almost completely clean (Schwarz 1981; Contopoulos & Papayannopoulos 1980). Since periodic orbits in a bar potential tend to be aligned parallel or perpendicular to the bar and achieve maximum local eccentricity in the principal resonance regions (Contopoulos 1979), then rings and pseudorings which form in these regions tend to be oval in shape and are aligned either parallel or perpendicular to the bar. This leads to significant noncircular motions, the amplitude of which can be used to measure the amplitude of the bar forcing.

Such effects ought to be most easily observed in the gas distributions of these galaxies, but so far, only a handful have been mapped in H I. Studies of the ringed galaxies NGC 1291 and NGC 5101 (van Driel, Rots, & van Woerden 1988), NGC 1365 (Jörsäter & van Moorsel 1995, hereafter JvM), NGC 1398 (Moore & Gottesman 1995), NGC 4725 (Wevers 1984), NGC 4736 (Mulder & van Driel 1993), NGC 5850 (Higdon & Buta 1996), and NGC 2273, NGC 4826, and NGC 6217 (van Driel & Buta 1991) have generally found concentrations of H I gas coincident with the optical rings and pseudorings, together with a pronounced central hole, at least as large as the bar (if present). However, none of these galaxies possess the full range of ring types, and a patchy knowledge of their kinematics has made it difficult to rigorously test the association between rings and resonances.

Until quite recently, two of the very best examples of ringed barred galaxies were inaccessible to existing aperture synthesis telescopes. The southern spiral NGC 1433, besides being one of the nearest, largest, and best presented examples, is also the prototype for the class of ringed, barred spiral galaxies. It possesses all of the three main ring types normally found (a nuclear ring/lens, an inner ring, and an outer pseudoring), as well as a remarkable pair of "plumes," or short spiral arcs symmetrically leading the bar. In a comprehensive study, Buta (1986b, hereafter B86) used multicolor surface photometry and H α Fabry-Perot inter-

ferometry to study the star formation and kinematic properties of these rings. On kinematical grounds, he was able to associate each of the ring features with the orbital resonances already mentioned. Owing to the rather localized distribution of ionized material, however, it was not possible to carry out a complete dynamical analysis. Of particular importance in that study was kinematic verification of the extreme intrinsically oval shape of the inner ring, and its alignment parallel to the bar. At the time of these observations, rings were thought to be nearly circular, and the significance of alignments was not yet appreciated (see Kormendy 1979, 1982).

Despite also being classed as an intermediate-type ringed barred spiral, NGC 6300 makes for an interesting contrast with NGC 1433, having a virtually identical angular size and distance. There is no nuclear ring, and the outer arms do not form an outer pseudoring (Buta 1987, hereafter B87). The inner ring is exceptionally broad and dusty and may in fact not be aligned parallel to the bar, as is the case for NGC 1433. The rotation curve, derived from optical emission-line spectra, shows evidence for noncircular motions in the bar, consistent with bar-driven gas inflow. Interestingly, the rotation curve within the optical disk is remarkably well predicted by the V-band light distribution, using only a single constant value for the mass-to-light ratio.

We have used the Australia Telescope Compact Array (ATCA) to map the H I line emission and the 1.38 GHz continuum emission in both these galaxies. In this paper, we describe the ATCA observations in § 2, present the results of our analysis in § 3, and then discuss our findings in relation to the resonance hypothesis in § 4. A list of fundamental and observational parameters for NGC 1433 and NGC 6300, along with new quantities derived by us in this study, is given in Table 1.

2. ATCA OBSERVATIONS

Both galaxies were observed using a number of separate ATCA configurations between 1994 March 2 and 1994 June 4, typically for ~ 12 hr each per configuration. The baselines employed spanned the range from 31 m to 1500 m. Some details of the observations are summarized in Table 1. For the H I observations, a bandwidth of 8 MHz was used, divided into 512 channels each covering 3.3 km s^{-1} , and

TABLE 1
OBSERVATIONAL AND DERIVED PARAMETERS FOR NGC 1433 AND NGC 6300

PARAMETER	GALAXY	
	NGC 1433	NGC 6300
Hubble type ^a	(R ₁)SB(rs)ab	SB(rs)b
Configurations.....	0.375, 0.75A, 0.75B, 1.5C	0.375, 0.75A, 0.75B, 1.5C, 1.5D
Total observation time.....	48 hr	58 hr
α (J2000 pointing center).....	03 ^h 42 ^m 01 ^s .2	17 ^h 16 ^m 58 ^s .2
δ (J2000 pointing center).....	- 47°13'18"	- 62°49'11"
FWHP synthesized beam ^b	33" \times 27" (1.86 \times 1.52 kpc)	25" \times 23" (1.72 \times 1.58 kpc)
Channel map rms noise ^b	0.9 mJy beam ⁻¹	1.0 mJy beam ⁻¹
Continuum map rms noise ^b	0.14 mJy beam ⁻¹	0.15 mJy beam ⁻¹
Distance adopted ^c	11.6 Mpc	14.3 Mpc
Inclination adopted.....	33°	(51° \pm 4°)
$M_B^{b,i}$	-19.21 \pm 0.33	-19.92 \pm 0.24
$M_{H\text{I}}$	(1.05 \pm 0.05) $\times 10^9 M_\odot$	(2.6 \pm 0.2) $\times 10^9 M_\odot$
$M_{H\text{I}}/L_B$	0.14 \pm 0.05 M_\odot/L_\odot	0.18 \pm 0.06 M_\odot/L_\odot

^a From the Catalog of Southern Ringed Galaxies (Buta 1995).

^b Uniform weighting.

^c Tully 1988.

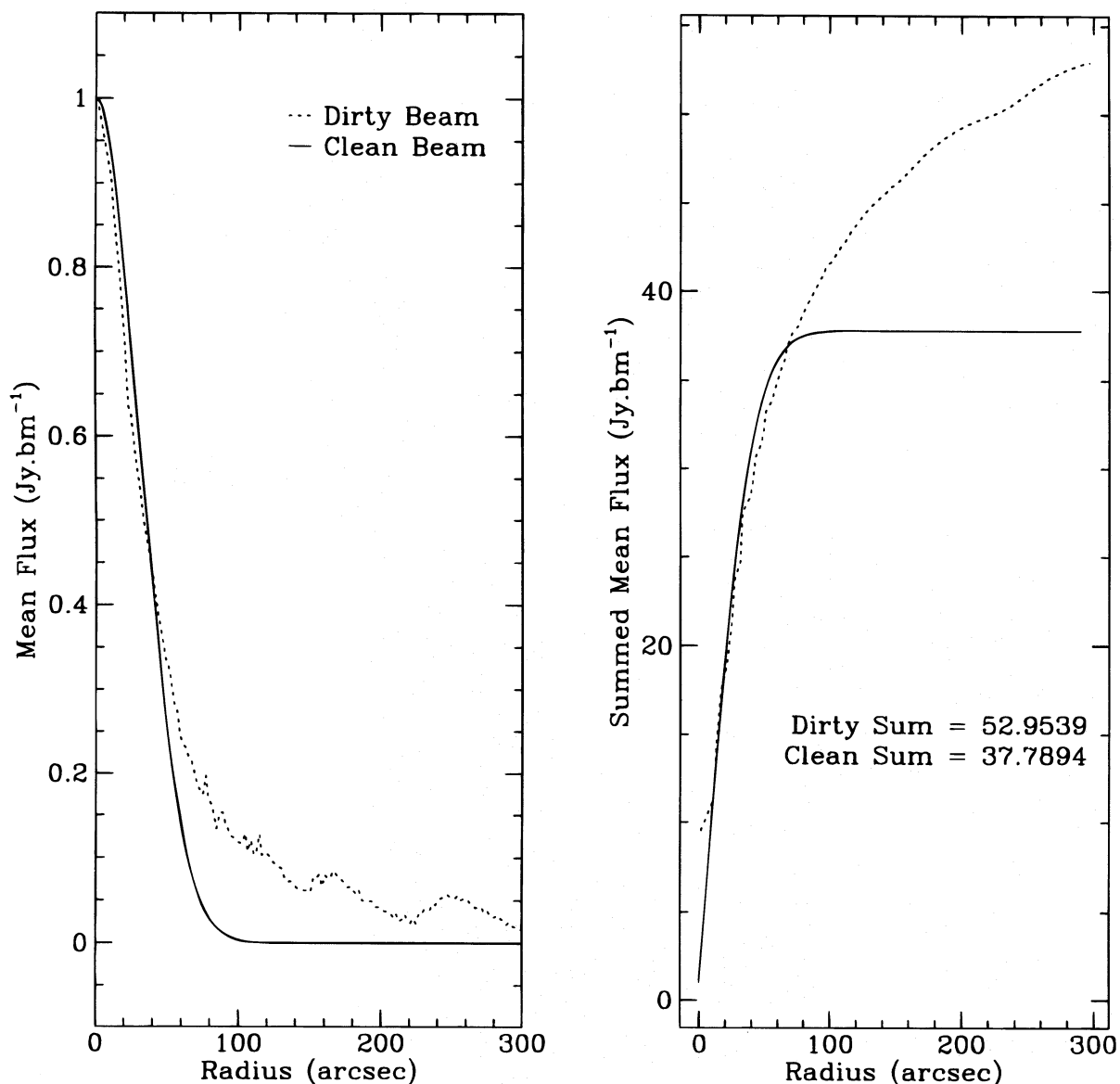


FIG. 1.—*Left*: Major axis radial profiles of the dirty (natural-weighted) beam and the best-fitting Gaussian clean beam used by AIPS. *Right*: The integrated flux within a given radius from each beam shape. The implications of the differences between the dirty and clean beams for image cleaning and total flux estimates are discussed in the paper by Jörsäter & van Moorsel (1995).

centered on a frequency of 1.415 GHz (corresponding to a heliocentric velocity in the optical convention to be used here of $c\Delta\nu/\nu = 1146 \text{ km s}^{-1}$). The systemic velocities of NGC 1433 and NGC 6300 as measured by Reif et al. (1982) with the Parkes telescope (1080 and 1110 km s^{-1} , respectively) are close enough that we were able to use the same observing parameters for both. The second IF was used to simultaneously record measurements of the continuum emission within a 32 channel/128 MHz bandwidth centered on 1.38 GHz.

The primary ATCA calibrator, PKS B1934–638, was normally observed at least once per 12 hr run, assuming a flux density of 16.2 Jy at 1.4 GHz.⁴ Each 40 minute scan of a galaxy was bracketed by short observations of a nearby secondary calibrator: PKS B0438–436 (~ 5.2 Jy at 1.4

⁴ The recent recalibration of the 1934–638 flux density scale by Reynolds (1994) would revise this value (and all subsequent fluxes and H I mass determinations) downward by 8%.

GHz) for NGC 1433, and PKS B1718–649 (~ 3.8 Jy at 1.4 GHz) for NGC 6300. Each uv database for a given configuration, galaxy, and IF (spectral line or continuum) was processed separately using implementations of the NRAO Astronomical Image Processing System (AIPS) package at the Australia Telescope National Facility and at the University of Alabama. After interactive removal of spurious data from both polarizations on each of the 10 baselines, the data were corrected for gain and phase variations, and then a bandpass calibration based upon observations of the primary calibrator was applied. The spectral line data were then processed to remove any underlying continuum, the original 20 s integrations were extended to 60 s by averaging, and finally, Doppler corrections were applied to bring the individual configurations to a common velocity reference frame.

Data from all the available configurations were combined together into a single uv plane (in the case of the continuum data) using bandwidth synthesis, or (in the case of the spec-

tral line data) channels were averaged together in groups of three, separated by 9.9 km s^{-1} . Each continuum map (or plane of a spectral line cube), consisting of 256×256 $10''$ pixels, was CLEANed until 1000 iterations were completed, or until the total cleaned flux density changed by less than 0.1% (usually the former). Two separate weighting schemes were employed: uniform weighting, yielding a synthesized beamwidth of $\sim 30''$, and natural weighting, giving a beam nearly twice as large, but with an expected improvement in surface brightness sensitivity. Figure 1 compares the response of the “dirty” natural-weighted beam with that of the restoring “clean” beam (in essence, a Gaussian fitted to the central peak of the dirty beam), as well as the integrated flux measured by each type of beam (see the appendix of JvM for a discussion of the effects of the beam shape on cleaning and integrated fluxes). After correcting the data cubes for the effects of primary beam

attenuation, moment maps (H I column density, velocity, and velocity width) were constructed using a mask derived from a spatially and spectrally smoothed version of each cube, and by setting a flux cutoff that just enabled a clean separation of the H I emission from background noise.

3. RESULTS

3.1. NGC 1433

3.1.1. H I Gas Distribution

Figure 2 shows each of the channel maps in the uniform-weighted cube, identified by their respective heliocentric velocities. To first order, NGC 1433 shows the characteristic pattern of uniform circular rotation, although there are clearly gaps in the H I distribution. To determine the extent to which we may be missing H I flux because of missing uv spacings (or perhaps overestimating the flux because of

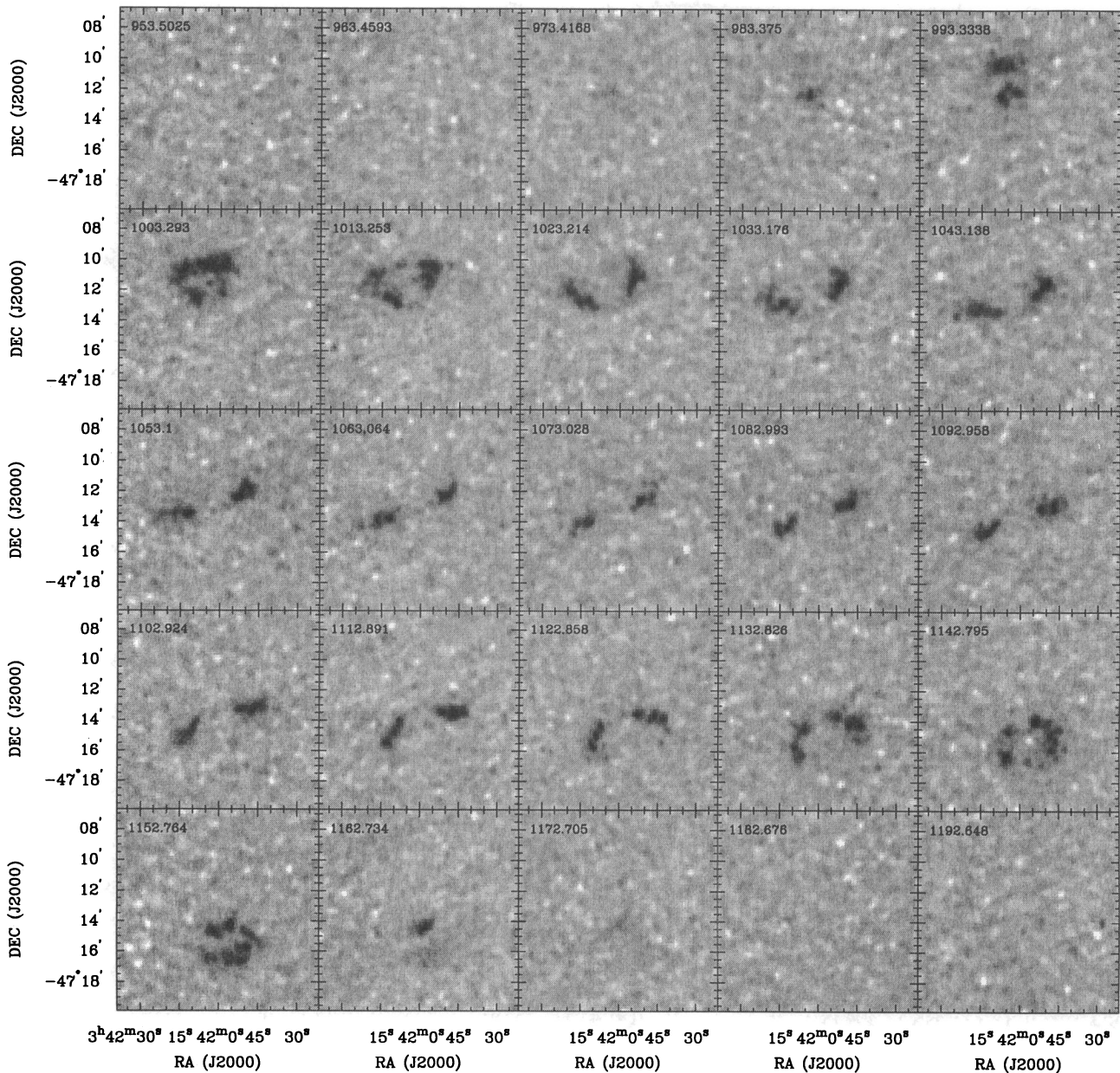


FIG. 2.—H I channel maps of NGC 1433 after CLEANing with a uniform-weighted beam. Heliocentric velocities in the optical convention are given in units of km s^{-1} . The darkest gray level corresponds to a flux density $\sim 15 \text{ mJy beam}^{-1}$.

inadequate cleaning; JvM), we have measured global H I profiles from both the uniform- and natural-weighted cubes, using a moving window to optimize the emission measured in each individual channel map. The two profiles are shown together in Figure 3, together with a new spectrum obtained recently by us with the Parkes 64 m telescope. Table 2 compares our measurements of the moments for each of these three global H I profiles.

Despite using a total of four array configurations to increase our sampling in the uv plane, we would still expect to resolve out some of the lowest surface brightness emission. Ryder et al. (1995), using a total of five ATCA configurations, found a 6% loss of total flux for the late-type barred spiral NGC 1313, compared with the integral from a grid of Parkes observations. The flux integral measured from the uniform-weighted cube is $32.2 \text{ Jy km s}^{-1}$, while that from the natural-weighted data is only slightly more at $34.4 \text{ Jy km s}^{-1}$. Both these flux integrals agree well with our new Parkes measurement, which represents nearly a 50% increase in total H I content over that measured by Reif et al. (1982) from a relatively poor signal-to-noise ratio spectrum of NGC 1433. Our Parkes spectrum has not been corrected for dilution by the primary beam, but the extent of the H I disk does not appear to be sufficient to cause

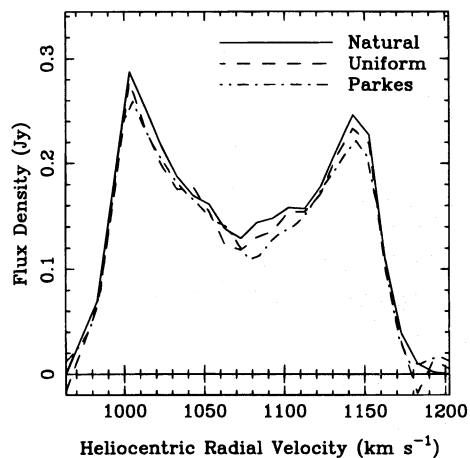


FIG. 3.—Global H I profiles of NGC 1433 obtained by measuring the pure emission within each plane of the uniform (*dashed line*) and natural (*solid line*) weighted cubes, corrected for primary beam attenuation. For comparison, the dash-dotted line is a recent spectrum from a single pointing with the Parkes 64 m antenna, not corrected for beam dilution.

overflowing of either the Parkes beam ($15'$ at 1.4 GHz) or the ATCA primary beam ($34'$).

Adopting a distance to NGC 1433 of 11.6 Mpc (Tully 1988, but see § 4.1) and assuming optically thin gas, our measurements of the flux integral in NGC 1433 yield a total H I mass of $(1.05 \pm 0.05) \times 10^9 M_{\odot}$. For an absolute blue magnitude of $M_B^{b,i=33} = -19.21 \pm 0.33$ (§ 4.1), the ratio $M_{\text{H I}}/L_B = 0.14 \pm 0.05 M_{\odot}/L_{\odot}$. This is well within the median range of H I mass-to-blue luminosity ratios found in Sab galaxies by Roberts & Haynes (1994), so that even though the distribution of gas and stars in NGC 1433 is somewhat unusual, the relative H I content is not.

Since we do not appear to be losing any significant emission by using uniform weighting, we shall discuss only the uniformly weighted data from here on. The global profile width at 20% of the peak level (W_{20}), uncorrected for either turbulent or instrumental broadening effects, is $190 \pm 10 \text{ km s}^{-1}$ (Table 2). Unlike the H I flux integral, this value is in extremely good agreement with that measured by Reif et al. (1982). We shall defer the conversion of W_{20} to a deprojected velocity width until § 4.1, after we have had a chance to consider the H I morphology and kinematics.

The H I column density distribution is shown as both a gray scale and as contours in Figure 4. The full width at half-power (FWHP) of the elliptical Gaussian restoring beam is shown in the lower left of this figure. The tight confinement of the neutral atomic hydrogen to both an inner and an outer ring is quite striking. Just how good the alignment really is between the gas and the stellar rings is best illustrated in Figure 5, where the H I column density contours have been overlain on a 600 s B -band CCD image of NGC 1433 obtained with the CTIO 1.5 m telescope. The B image has been placed on a logarithmic scale in order to bring out the faint outer pseudoring as well as the inner ring, bar, and nuclear ring. Comparison of Figure 5 with Figure 4 shows that both the inner and the outer stellar rings are almost perfectly aligned with their atomic gas counterparts. The gas density peaks near the ends of the bar, where it joins the major axis of the aligned inner ring. Neutral gas is deficient in the bar itself but appears to build up again at a point just slightly to the east of the optical nucleus (which is itself virtually coincident with the dynamical center as determined in § 3.1.2). Secondary peaks of H I surface density are seen to underlie both the “plume” features discussed by B86. Areas in between the bar and the inner ring, and especially regions between the inner ring

TABLE 2
GLOBAL H I PROFILE PARAMETERS

Profile Source	Integral Flux Density (Jy km s^{-1})	Systemic Velocity (km s^{-1})	W_{20} (km s^{-1})
NGC 1433			
Natural	34.4	1075	191
Uniform	32.2	1075	188
Parkes (this study).....	31.4	1074	191
Parkes (Reif et al. 1982).....	23.6	1080	191
NGC 6300			
Natural	55.0	1110	317
Uniform	51.0	1111	314
Parkes (Mazzolini et al. 1996).....	57.2	1110	320
Parkes (Reif et al. 1982).....	61.0	1110	341

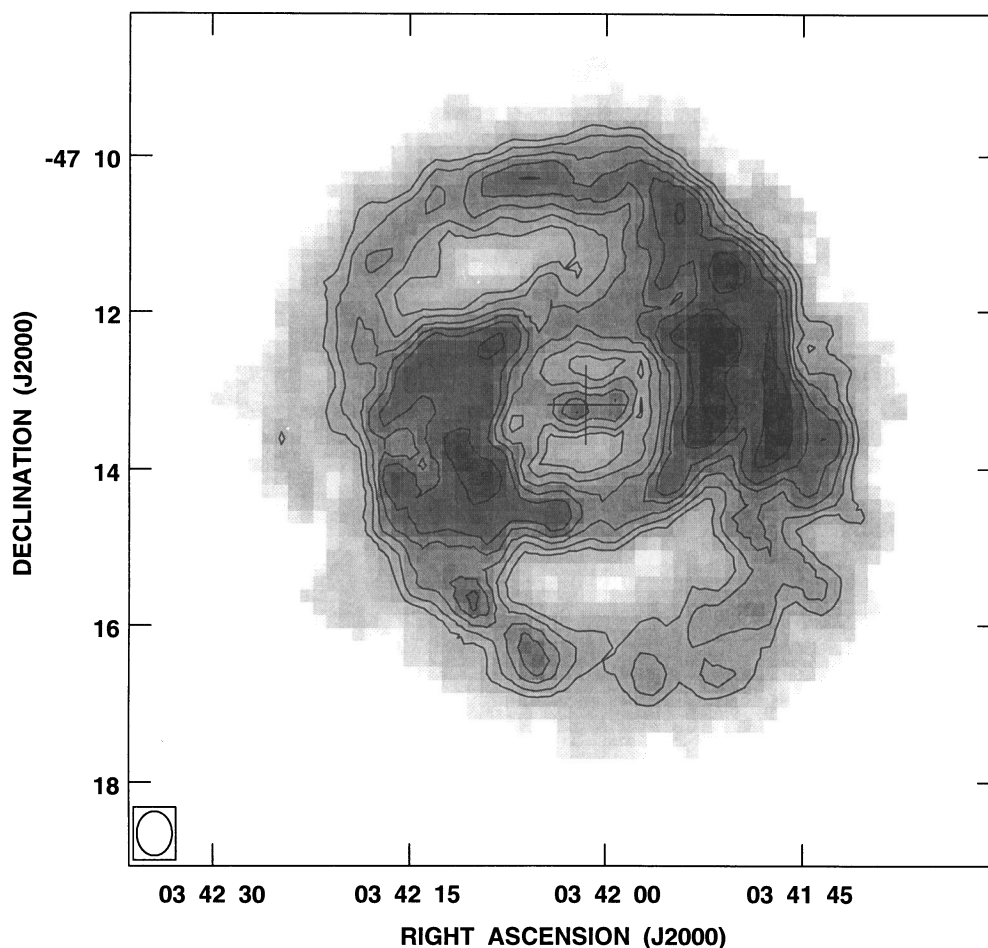


FIG. 4.—Gray-scale and contours of H I column density in NGC 1433. Contours represent (projected) column densities of 1.4, 1.9, 2.5, 3.2, 3.8, 5.0, and $6.3 \times 10^{20} \text{ cm}^{-2}$. The FWHP of the synthesized beam is shown by the ellipse in the bottom left corner. The cross marks the position of the dynamical center.

minor axis and the outer pseudoring, are relatively devoid of neutral hydrogen.

The azimuthally averaged radial variation of the H I column density has been calculated using the IRING task, by assuming an inclination of 33° (§ 4.1) and other disk parameters taken from the kinematical analysis (§ 3.1.2). The radial profile of H I, corrected to face-on, is shown in Figure 6. Also marked in this figure by dashed lines are the mean apparent radii for the various morphological features, as tabulated by B86. The H I surface density starts from a peak of $2 M_\odot \text{ pc}^{-2}$ in the nucleus and drops to as low as $1 M_\odot \text{ pc}^{-2}$ along the bar, before reaching its highest value of some $2.5 M_\odot \text{ pc}^{-2}$ just outside the mean radius of the inner ring. Despite localized H I peaks underlying the plumes, the mean gas surface density at their radial distance is lower overall because of the “missing” gas in the inter-ring region. The H I column density reaches one more peak at or just beyond the radius of the outer pseudoring, before declining quasi-exponentially thereafter. We perhaps ought not to be too surprised to find peaks in the gas surface density just outside the stellar rings, as neither can exist precisely at the resonant orbit radii. In the rush to escape the unstable resonant orbits, the gas clouds collide, form new stars, and lead to an eventual buildup in stellar surface density near to, *but not right at*, the resonance radii. We note in passing that the outermost point at which the H I surface density drops to a level of $1 M_\odot \text{ pc}^{-2}$ corresponds to a distance of $1.18R_{25}$ ($R_{25} = D_{25}/2$), quite typical for

Sa–Sab galaxies (Warmels 1986) despite the perturbing actions of the bar and its associated resonances.

3.1.2. H I Kinematics

The H I velocity field, as determined from the moment analysis, is shown superimposed on the gas column density map in Figure 7. Owing to the low gas densities in the outskirts of the disk, and between the inner and outer rings, we have been forced to mask out many unreliable data points in these areas. Even so, we can still get a good feel for how complex the velocity field in this particular galaxy really is. The “spider” pattern characteristic of disks in uniform circular rotation is still evident, but modulated heavily by the nonuniform gas distribution and apparent departures from circular motion. There is an exceptionally steep velocity gradient along the central $1'$ or so of the kinematic major axis (roughly perpendicular to the bar), with severe distortions along the southern edge of the optical bar. Further out along the major axis, the iso-velocity contours close up when they reach the inner ring, implying that the projected rotational velocity reaches a maximum there and then begins to drop. Somewhat perversely, a lack of gas between the inner and outer rings with which to trace the motions makes the velocity field somewhat chaotic in this important transition region. Fortunately, there is plenty of gas along the kinematic minor axis, although there the correction for deprojection will introduce a large uncertainty. In regions of high gas surface

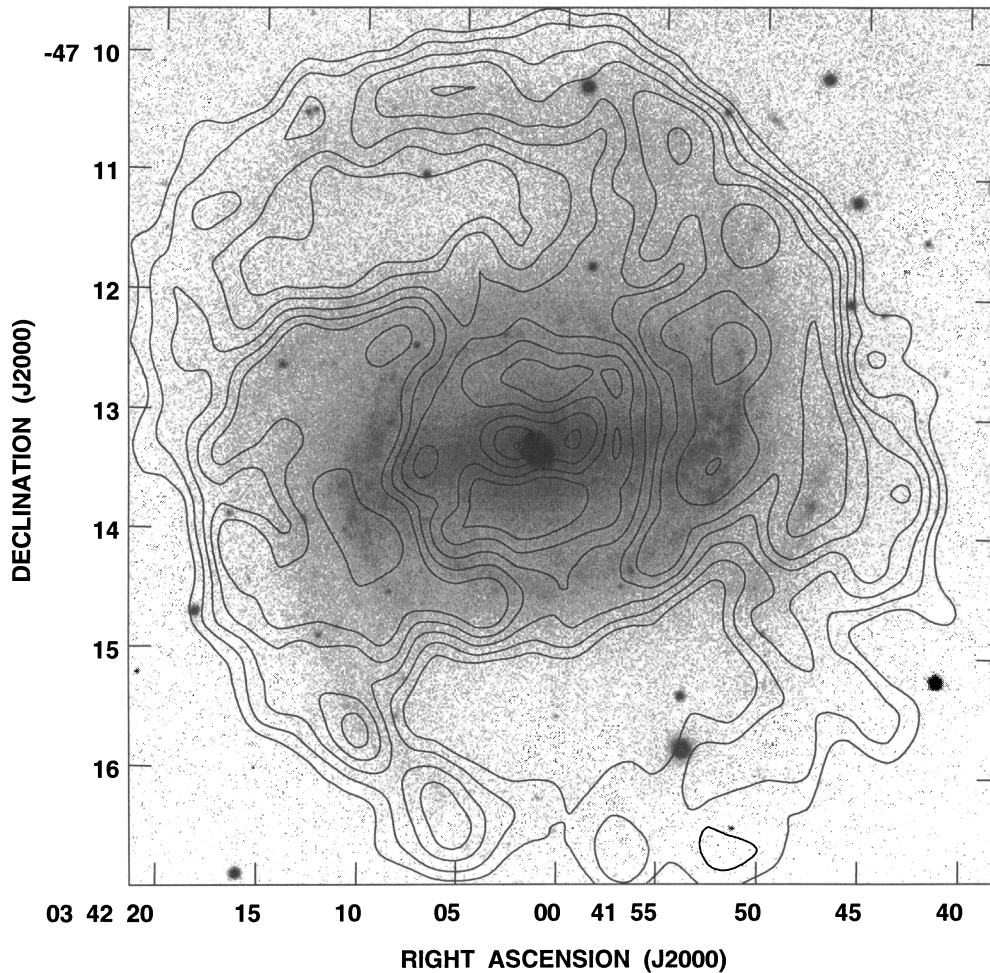


FIG. 5.—Contours of the H I column density overlain on a *B*-band image of NGC 1433. The contour levels are the same as for Fig. 4 but have been regridded to match the pixel scale of the optical image. The *B*-band intensity has been displayed on a logarithmic scale, in order to make both the outer pseudoring and nuclear detail visible.

density, there are kinks indicative of noncircular motions, but with no systematic pattern to them.

We have attempted to determine a rotation curve from the velocity field using an implementation of the ROTCUR algorithm (Begeman 1987) within AIPS to fit elliptical rings

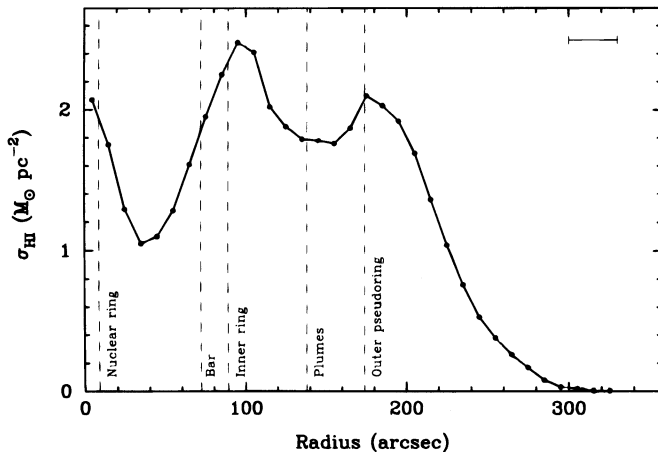


FIG. 6.—Radial distribution of the azimuthally averaged H I surface density, corrected to face-on, assuming a disk inclination of 33° and optically thin gas. The mean radii of prominent optical features, as measured by Buta (1986b), are indicated by the dashed lines. The bar at top right denotes the approximate FWHM beamwidth.

of varying inclination and position angle. As starting values for the kinematical parameters (dynamical center position, systemic velocity, and disk tilt and position angle), we adopted the numbers arrived at by B86 in his photometric and optical interferometric study of NGC 1433. However, the gas deficiencies along the major axis, as well as the need to exclude velocity points within $\pm 25^\circ$ of the minor axis, tend to result in convergence toward unreasonably small values for the disk inclination (and correspondingly excessively large deprojected rotation velocities) if all the parameters are allowed to vary freely. The only way to obtain a satisfactory fit to the velocity field is to assume a priori a constant inclination for the gas orbits at all radii.

By assuming the outer isophotes are intrinsically circular, B86 arrived at an inclination of $i = 33^\circ$. On the other hand, statistics from the Catalog of Southern Ringed Galaxies (Buta 1995, hereafter CSRG) indicate that outer ring features in strongly barred galaxies have, *on average*, an intrinsic axial ratio of 0.82 ± 0.07 . For this reason, and others to be discussed in § 4.1, he conceded that the actual inclination of NGC 1433 to the plane of the sky could be as low as 20° or so. Figure 4 is not immediately helpful in regard to settling this matter, owing to the way the gas is so clearly organized into these same rings. The lowest contour in Figure 4 ($1.1 M_\odot \text{ pc}^{-2}$) spans roughly 7.5×6.3 (25×21 kpc at a distance of 11.6 Mpc), yielding an axial ratio

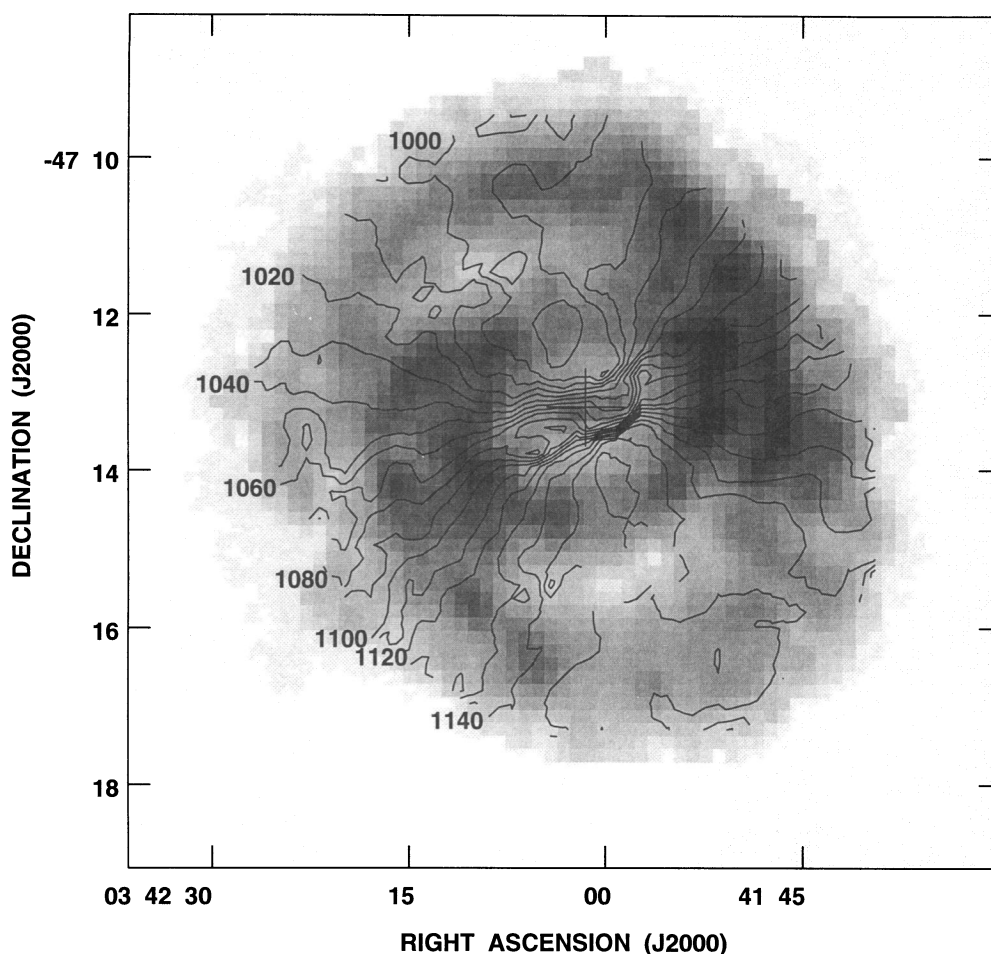


FIG. 7.—Isovelocity contours overlain on the H I column density map of NGC 1433. The contours are at intervals of 10 km s^{-1} , and major velocity contours are marked. The closed contours along the kinematic major axis correspond to heliocentric velocities of 990 km s^{-1} (top) and 1160 km s^{-1} (bottom). Many spurious velocity points around the edge of the disk and around the vacant southern region have been blanked out because of poor signal-to-noise ratio. The cross marks the position of the dynamical center, as determined from the ROTCUR analysis (see text).

$q = 0.84$, wholly consistent with the isophote axis ratio $q = 0.85$ measured by B86.

Regardless of whether the inclination is held fixed at either 33° or at 20° , the ROTCUR analysis does produce consistent results for all the other parameters, if they are allowed to vary freely. We find a systemic velocity $V_{\text{hel}} = 1075 \pm 2 \text{ km s}^{-1}$, and a kinematic major axis position angle of $\theta = 201^\circ \pm 1^\circ$. These results compare quite favorably with the equivalent parameters determined by B86 from his optical kinematic modeling: $V_{\text{hel}} = 1079 \pm 2 \text{ km s}^{-1}$ and $\theta = 197^\circ$, and with the systemic velocities measured from the global H I profiles (Table 2). The dynamical center of the H I disk lies at $\alpha_{\text{dyn}}(\text{J2000}) = 03^{\text{h}}42^{\text{m}}1^{\text{s}}.5 (\pm 10'')$, $\delta_{\text{dyn}}(\text{J2000}) = -47^\circ 13' 12'' (\pm 5'')$. Within the error bars, this is virtually coincident with the position of the optical nucleus as given by de Vaucouleurs et al. (1991, hereafter RC3). As mentioned in the previous section, the central peak in the H I distribution is offset to the east of the dynamical center, though by less than one synthesized beamwidth.

In § 4.1, we demonstrate that the most plausible inclination for the disk of NGC 1433 as a whole is of order 33° . By holding all other parameters fixed as above, and finding the mean rotational velocity within annuli of increasing semi-major axis, we have compiled separate rotation curves for the approaching and receding halves, as well as for the disk

as a whole. Figure 8 shows plots of these deprojected rotation velocities. Any differences between the two halves are a better reflection of velocity uncertainties than the formal fitting errors. Clear asymmetries in the velocity field around the bar visible in Figure 7 lead to a large spread in possible values within the first $1'$ or so, but further out, agreement between the approaching and receding halves improves rapidly. After an extremely steep rise to a maximum rotational velocity of about 170 km s^{-1} just inside the bar/inner ring region, the rotation curve levels off at just on 150 km s^{-1} , even as it passes the radius of the outer pseudoring ($174''$; B86). A model velocity field was constructed from the full-disk rotation curve and subtracted from the observed velocity field. The rms residuals are only of order 10 km s^{-1} but exhibit roughly a $\sin 3\phi$ variation with azimuthal angle ϕ , suggesting that a fixed inclination of 33° may still not be appropriate everywhere in the disk.

If anything, the central velocity gradient is likely to be even steeper than shown in Figure 8, owing to the smoothing effect of our $\sim 30''$ beam. H α Fabry-Perot kinematics would be an ideal complement to the H I velocity field, adding spatial resolution where it is needed most. Unfortunately, the predilection of the H II regions for the inner and nuclear rings alone made it impossible for B86 to trace the velocity field in between these rings. With the increased sensitivity of modern instrumentation to lower surface

brightness emission however (e.g., Bland-Hawthorn et al. 1994), it may yet be possible to derive kinematical information from this critical region.

3.1.3. Radio Continuum

As part of a general imaging program of southern ringed galaxies, Crocker, Baugus, & Buta (1996) have used the CTIO 1.5 m telescope to obtain images in the narrowband H α and adjacent red continuum. Figure 9 shows a 1200 s continuum-subtracted H α image of NGC 1433, on which has been overlain contours of the 1.38 GHz continuum emission (uniform-weighted) observed with the ATCA. Not surprisingly, most of the radio continuum contours outline quite well the star-forming complexes found at each end of the bar, as well as the plumes and the nuclear ring. The integrated flux densities from the H II region complexes at the eastern and western ends of the bar are found to be 3.4 mJy and 3.7 mJy, respectively, comparable to the total nuclear flux density of 3.4 mJy. In the absence of observations at a second frequency, we can only speculate on the source of this emission, but we expect that any nonthermal component will dominate the continuum emission at 1.38 GHz (Condon 1992). Thus, the concentrated emission originating near the ends of the bar and the inner ring minor axis is presumably associated more with supernovae (and/or focusing of the magnetic field lines because of the

orbit crossings there) than with the enhanced star formation activity that eventually gives rise to the supernova activity. Radio continuum emission is much sparser in the outer pseudoring, as indeed is the number of H II regions. The

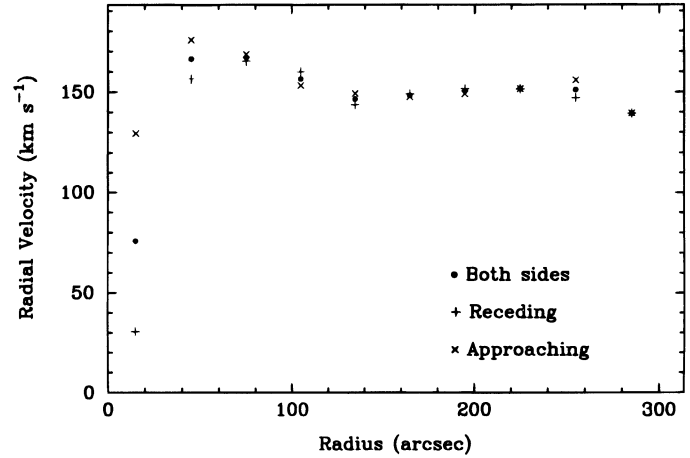


FIG. 8.—H I rotational velocities derived from the velocity field, assuming circular motion in rings inclined at 33° , with rotation center, systemic velocity, and position angle held fixed at the values given in the text. The points are plotted at 1 beamwidth intervals, based on separate fits to the receding (i.e., mostly the southern) half, the approaching (northern) half, and to the entire disk. The formal fitting errors are usually much less than the differences between these three fits.

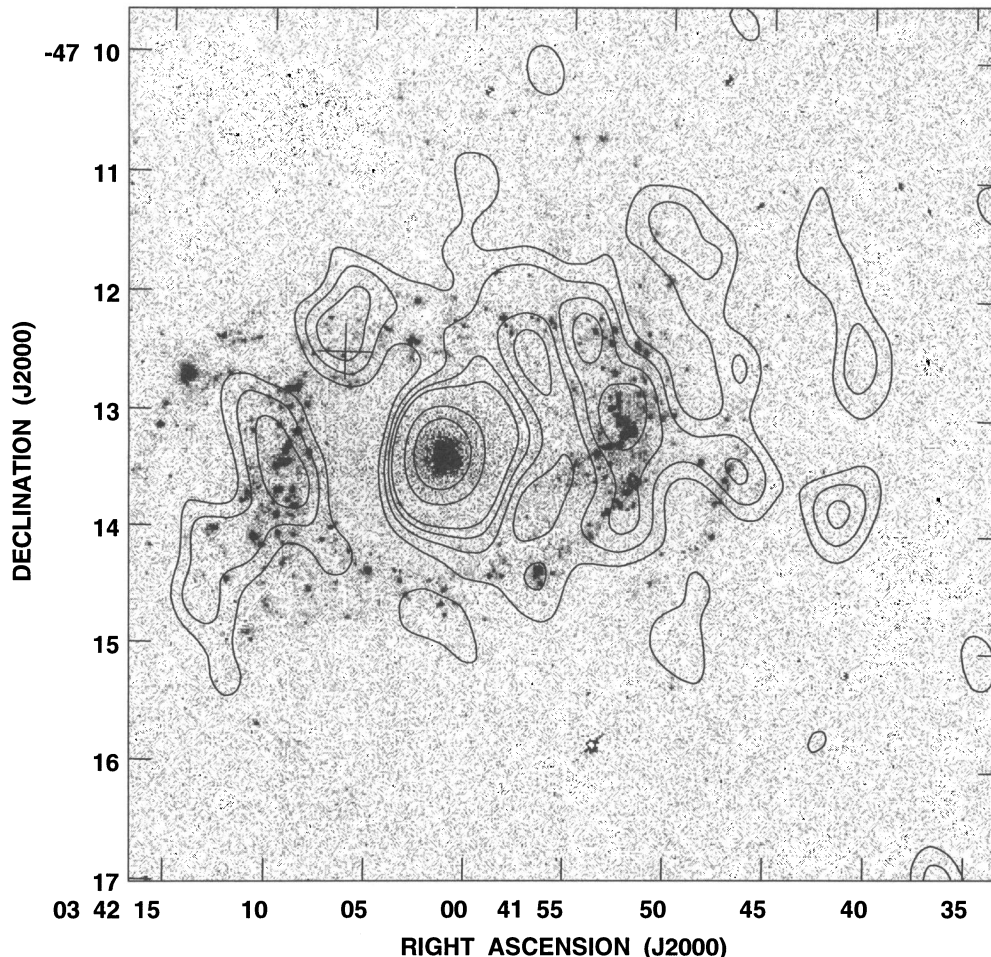


FIG. 9.—Contours of 1.38 GHz continuum flux density overlain on a 1200 s continuum-subtracted H α image obtained by D. Crocker and G. Purcell with the CTIO 1.5 m telescope. The radio continuum contours are at levels of 0.4, 0.6, 0.8, 1.0, 2.0, and 3.0 mJy beam $^{-1}$. The cross '1' northeast of the nucleus marks the approximate optical position of the Type II supernova SN 1985P discovered by R. Evans.

origin of the westernmost arc of continuum emission is unclear, as it lies outside any optical or H I feature.

A growing number of Type II supernovae have now been detected as radio and X-ray sources within 10–20 yr of the optical outburst, e.g., SN 1986J (Rupen et al. 1987) and SN 1978K (Ryder et al. 1993). The cross in Figure 9 to the northeast of the nucleus of NGC 1433 marks the best-known optical position of the Type II supernova SN 1985P (Barbon, Cappellaro, & Turatto 1989). Within the 30" beam size, this cross coincides with the peak of an extended patch of emission along the inner ring of NGC 1433 and at least one weak H α source. Although this identification is far from definite, we can at least place an upper limit on the integrated flux density of SN 1985P at the current epoch as $S_{1.38\text{ GHz}} \lesssim 0.5$ mJy. This places SN 1985P at least an order of magnitude fainter than the "normal" Type II radio supernova SN 1979C at the equivalent point in its radio evolution, and well short of the luminosities attained by the "peculiar" radio supernovae exemplified by SN 1986J and SN 1978K (Weiler et al. 1995). Based upon our present understanding of the evolution of young and intermediate-age supernova remnants (e.g., Chevalier & Fransson 1994), such a low radio luminosity nearly a decade after outburst would require a relatively low progenitor mass-loss rate and a correspondingly rarefied circumstellar medium for the expanding supernova to interact with.

3.2. NGC 6300

3.2.1. H I Gas Distribution

As was the case with NGC 1433, contour plots of the uniform-weighted channel maps of NGC 6300 (Fig. 10) are, to first order, consistent with uniform circular motion, but they hint at a nonuniform surface density distribution and some kinematic irregularities in the outer disk. Before examining the moment maps formed from these channel maps, we ought to again compare the global H I profiles from the uniform- and natural-weighted data sets with an equivalent Parkes spectrum, kindly supplied to us by M. Mazzolini. All three profiles are shown together in Figure 11 and display remarkably good agreement in profile width, alignment, and structure. Table 2 shows just how well our synthesis measurements compare with single-dish observations.

Once again, our uniform- and natural-weighted cubes yield integrated H I fluxes that agree to better than 10% and come in only slightly below the two Parkes fluxes. The new Parkes spectrum has not been corrected for dilution caused by overfilling of the primary beam, which may be a much more significant effect than in NGC 1433, given the larger angular extent of the gas disk in NGC 6300 (Fig. 12). Although we could still be missing up to 15% of the total flux from NGC 6300, we note that all three spectra in Figure 11 outline the double-horned profile of NGC 6300 much better than does the spectrum published by Reif et al. (1982). Since most of the low surface brightness gas is expected to lie in the flat regime of the rotation curve that gives rise to these strong horns, it would not appear as though we are resolving out significant quantities of this gas. Adopting as the distance to NGC 6300 a figure of 14.3 Mpc (Tully 1988), we therefore estimate an H I gas content for NGC 6300 of $(2.6 \pm 0.2) \times 10^9 M_{\odot}$. Thus, NGC 6300 has at least twice as much neutral hydrogen as NGC 1433, and yet $M_{\text{H I}}/L_B = 0.18 \pm 0.06 M_{\odot}/L_{\odot}$, almost identical to the ratio found in NGC 1433 (§ 3.1.1).

Although the uniform-weighted data set does not appear to lose significant amounts of H I flux, our moment analysis has revealed that the resultant map of H I surface brightness fails to include some important low surface brightness features. We show in Figure 12 the gray scale and contours of the projected gas column density in NGC 6300, using a natural weighting of the uv data set that results in a broader synthesized beam ($\sim 50''$ as shown in the lower left corner) but an enhanced sensitivity to faint, extended structure. Just as we found in NGC 1433, there are clear peaks in the gas density, apparently associated with the optical stellar ring. However, in contrast to NGC 1433, there do not appear to be significant regions of the gas disk which have been swept clean of gas, even allowing for the increased projection effects owing to the higher inclination of NGC 6300. Furthermore, a natural-weighted map of the H I column density in NGC 1433 did not show such a ragged outer disk as NGC 6300, nor did it show any feature resembling the loose "tail" of gas seen emanating from the western edge of the gas disk of NGC 6300. Although this feature is barely separable from the background noise, a check of the associated velocity field confirms it to be a natural extension of the main gas disk. A search of the NASA Extragalactic Database turned up no interacting companion candidates within a 30' radius of NGC 6300, suggesting that this feature is associated with ongoing gas accretion rather than the remnant of a past close interaction. The same velocity field also confirms the visual impression from Figure 12 of a slight clockwise twist in the disk major axis in going from the ring to the disk edge. The case for a warp in the disk of NGC 6300 is examined more closely in § 3.2.2.

For the purposes of comparing the H I column density distribution in NGC 6300 with its kinematics and stellar distribution, we shall return to maps made from uniform-weighted data, which must sacrifice some low surface brightness sensitivity for the fullest possible resolution. Figure 13 shows contours of this high-resolution gas column density map superimposed on a 600 s *B*-band CCD image of NGC 6300. This image was also obtained with the CTIO 1.5 m telescope and is displayed here on a logarithmic scale, so as to bring out the outer optical disk, the inner ring, and the bar (the latter partly obscured by dust lanes and by two bright field stars). Here again, a stellar ring has been shown to have an H I counterpart, although the gas peaks in this ring appear to sit just slightly *outside* the ridge line of the optical ring. Notice also that a number of short spiral arcs, which are just discernible in the optical image extending from the outside of the ring, also have underlying H I counterparts, in particular, one that emerges from the eastern end of the disk major axis and wraps its way toward the west.

The gas disk as shown in Figure 12 spans approximately $14' \times 8'$ (a 60 kpc diameter at 14.3 Mpc), not including the tail. The run of deprojected H I column density with radius for the uniform-weighted map is shown in Figure 14 in which the ellipse geometries have been varied with radius according to the best-fit rotational model of the velocity field (§ 3.2.2). Although NGC 6300 has the same central density of H I as NGC 1433, it soon rises to over $4 M_{\odot} \text{ pc}^{-2}$ in the ring, nearly twice the maximum gas density seen in NGC 1433. Although neither the peak of the gas ring nor the full extent of the optical ring are particularly well defined, the H I ring is clearly much broader than the stellar ring and has a mean diameter closer to 70" as compared to

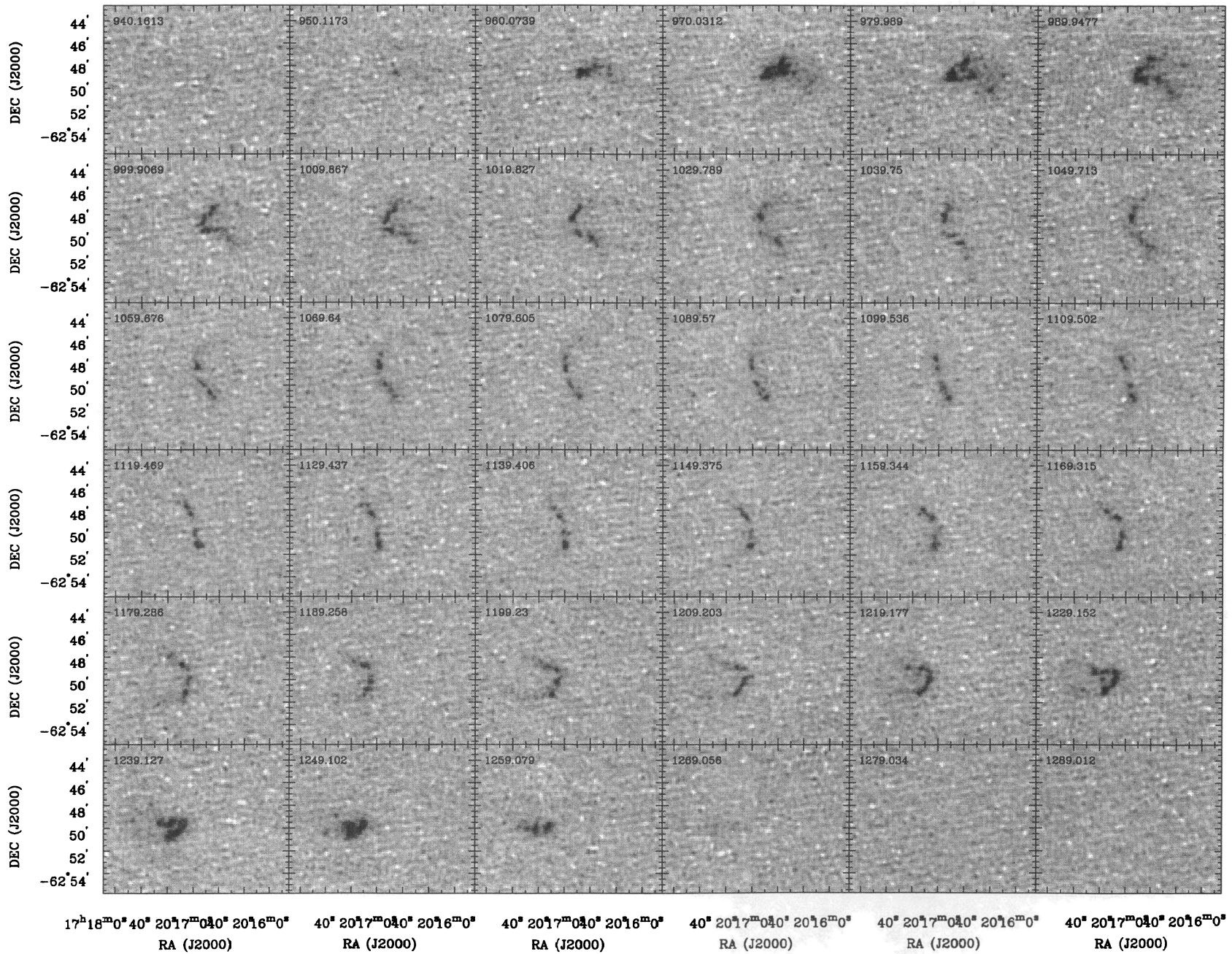


FIG. 10.—H I channel maps of NGC 6300 after CLEANing with a uniform-weighted beam. Heliocentric velocities in the optical convention are given in km s^{-1} . The darkest gray level corresponds to a flux density $\sim 40 \text{ mJy beam}^{-1}$.

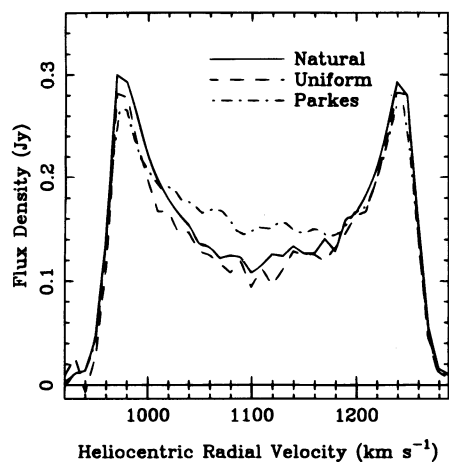


FIG. 11.—Global H I profiles of NGC 6300 obtained by measuring the pure emission within each plane of the uniform (*dashed line*) and natural (*solid line*) weighted cubes, corrected for primary beam attenuation. For comparison, the dash-dotted line is a spectrum from a single pointing with the Parkes 64 m antenna, which has not been corrected for beam dilution.

the optical ring diameter of $59''$ (B87; CSRG). The small peak at $145''$ most likely reflects the southern H I spur mentioned in the previous paragraph, although this spike is smaller than our beamwidth, and the ring inclination is changing rapidly in this region. From there, the H I column density slowly ramps down to our flux cutoff just past the H I tail, with no other candidates for a secondary peak that could indicate a subtle outer ring or pseudoring. Finally, we

observe that the H I surface density falls below $1 M_{\odot} \text{pc}^{-2}$ at a distance of $1.76R_{25}$, significantly larger than in NGC 1433 or for Sb galaxies in general.

3.2.2. H I Kinematics

Figure 15 shows isovelocity contours of the velocity field, overlain upon a gray-scale image of the H I column density, both of them constructed from the natural-weighted data. The kinematics of the gas tail are consistent with an extrapolation of the $1020\text{--}1080 \text{ km s}^{-1}$ contours from the main disk. Our early suspicions about a possible kinematic warp in the outer gas disk of NGC 6300 are also confirmed by this figure. Closed contours at 980 and 1240 km s^{-1} indicate that the projected rotational velocity reaches a maximum somewhere outside the radius of the ring.

At the resolution of this natural-weighted data ($\sim 50''$), there is little indication of the noncircular motions detected by B87 either in the bar, or elsewhere in the disk. Our best possible resolution comes from the uniform-weighted uv data set, and Figure 16 shows a close-up of the inner $6' \times 4'$ of NGC 6300, with H I column densities and isovelocity contours from this data set. Although the bending of the isovelocity contours in the inner $1'$ is consistent with the pattern of the optical isovelocity contours in Figure 12 of B87, these kinks do not extend much beyond the bar region, or across the ring itself. Thus, at the limited resolution of our H I data, the bar-driven gas inflow usually invoked to account for these noncircular motions appears to be confined within the bar region itself, although it is worth noting

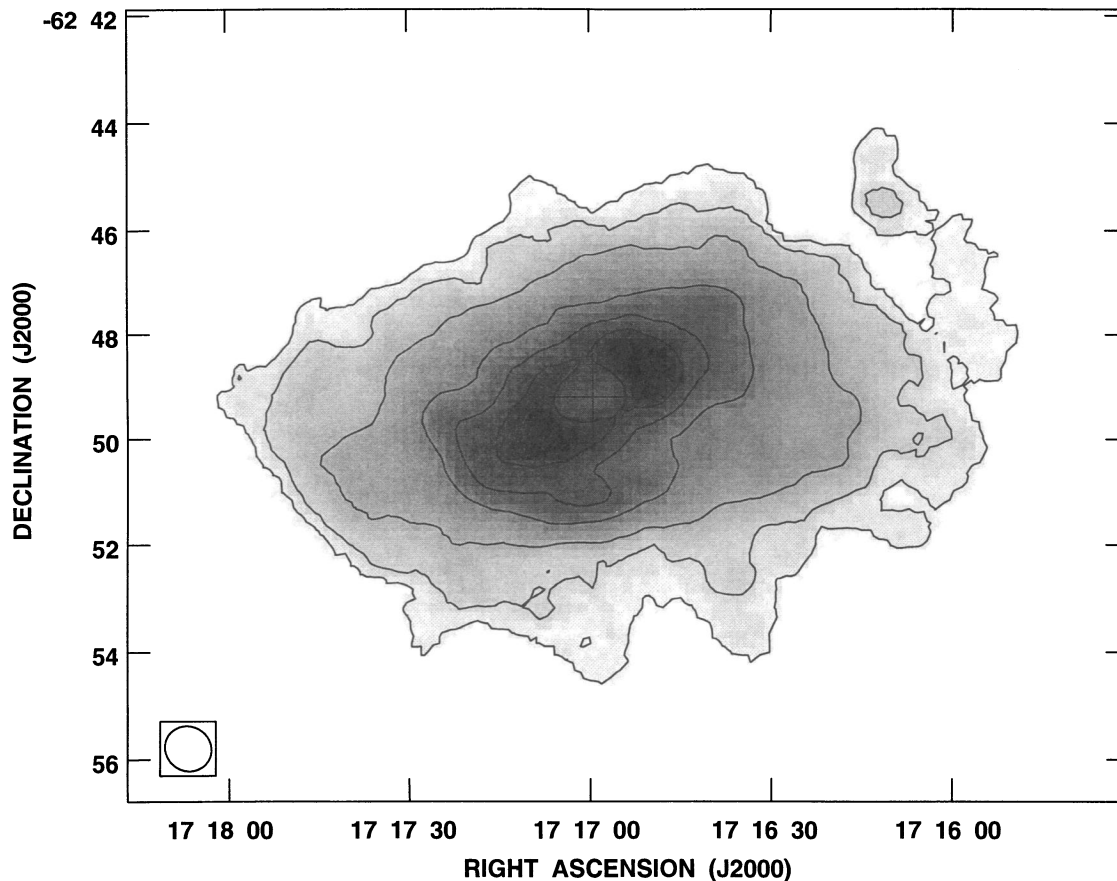


FIG. 12.—Gray-scale and contours of H I column density in NGC 6300, with natural weighting applied to the uv data. Contours represent (projected) column densities of $0.1, 0.5, 1.4, 3.7, 5.5, 7.3,$ and $9.2 \times 10^{20} \text{ cm}^{-2}$. The FWHM of the synthesized beam is shown by the ellipse in the bottom left corner. The cross marks the position of the dynamical center.

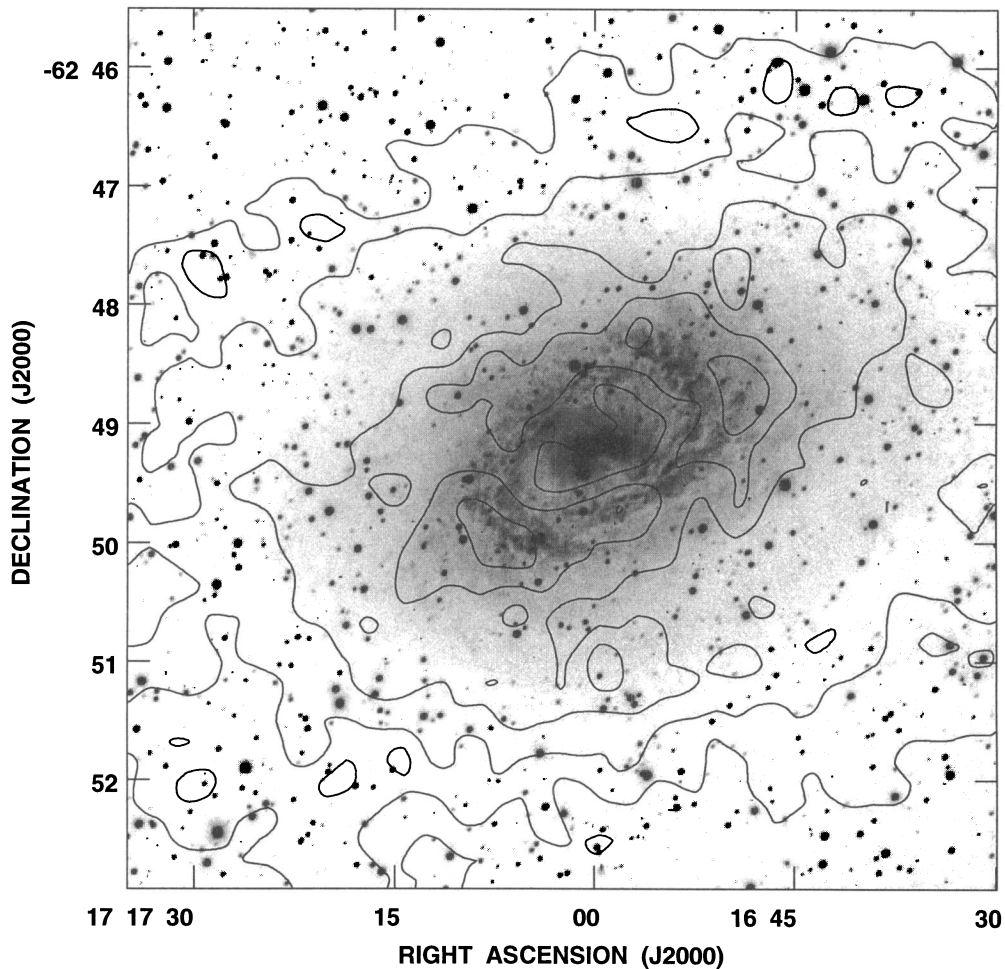


FIG. 13.—Contours of the H I column density overlain on a *B*-band image of NGC 6300. The contour levels are at projected column densities of 0.6, 2.0, 4.9, 7.9, and $10.8 \times 10^{20} \text{ cm}^{-2}$. The optical nucleus appears to be elongated, owing to the presence of a bright foreground star due west of the nucleus and another just to the southeast.

that the H I ring would provide a convenient reservoir of gas to sustain this process.

Because of the high projected gas column densities over the disk of NGC 6300 compared to NGC 1433, it was pos-

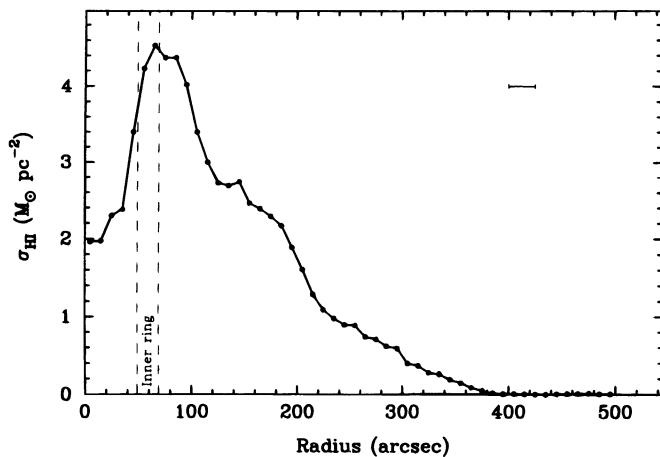


FIG. 14.—Radial distribution of the azimuthally averaged H I surface density, corrected to face-on, for which the shape of each ring (inclination and position angle) is set by the rotation curve fitting (Fig. 17). The approximate inner and outer boundaries of the inner ring, as given by Buta (1987), are indicated by the dashed lines. The bar at top right denotes the approximate FWHP beamwidth.

sible to carry out a full kinematical analysis of the uniform-weighted velocity field with ROTCUR that allowed both the inclination i and the position angle θ to be fitted as free parameters. After initially letting all parameters vary freely, we found the systemic velocity to remain steady at $V_{\text{hel}} = 1109 \pm 4 \text{ km s}^{-1}$, and a consistent dynamical center located at $\alpha_{\text{dyn}}(\text{J2000}) = 17^{\text{h}}16^{\text{m}}59^{\text{s}}.5 (\pm 4'')$, $\delta_{\text{dyn}}(\text{J2000}) = -62^{\circ}49'13'' (\pm 4'')$. Our redshift is in excellent agreement with other H I measurements (Table 2) and with the optical velocity of $1107 \pm 5 \text{ km s}^{-1}$ (B87). Our dynamical center is also identical with the nuclear position listed in RC3, although our H I data still lack the spatial resolution necessary to confirm the $5''$ displacement noted by B87.

Having locked the systemic velocity and the rotation center at these values, the kinematical analysis was repeated to determine the optimum position angle, inclination, and resultant deprojected rotational velocity at $25''$ (1 beamwidth) intervals, and the results are plotted in Figure 17. As with NGC 1433, fits were done on the disk as a whole, as well as for the separate halves, in order to quantify the extent of any disk asymmetry. The residuals of the fitted velocity field from that actually observed have a tendency to be mainly positive in the gas ring, and negative in the extended gas disk, but in both these regions, the rms amplitude of these residuals seldom exceeds 10 km s^{-1} .

We also have here a rare opportunity to compare directly a rotation curve for the H I with that of the ionized gas (H α)

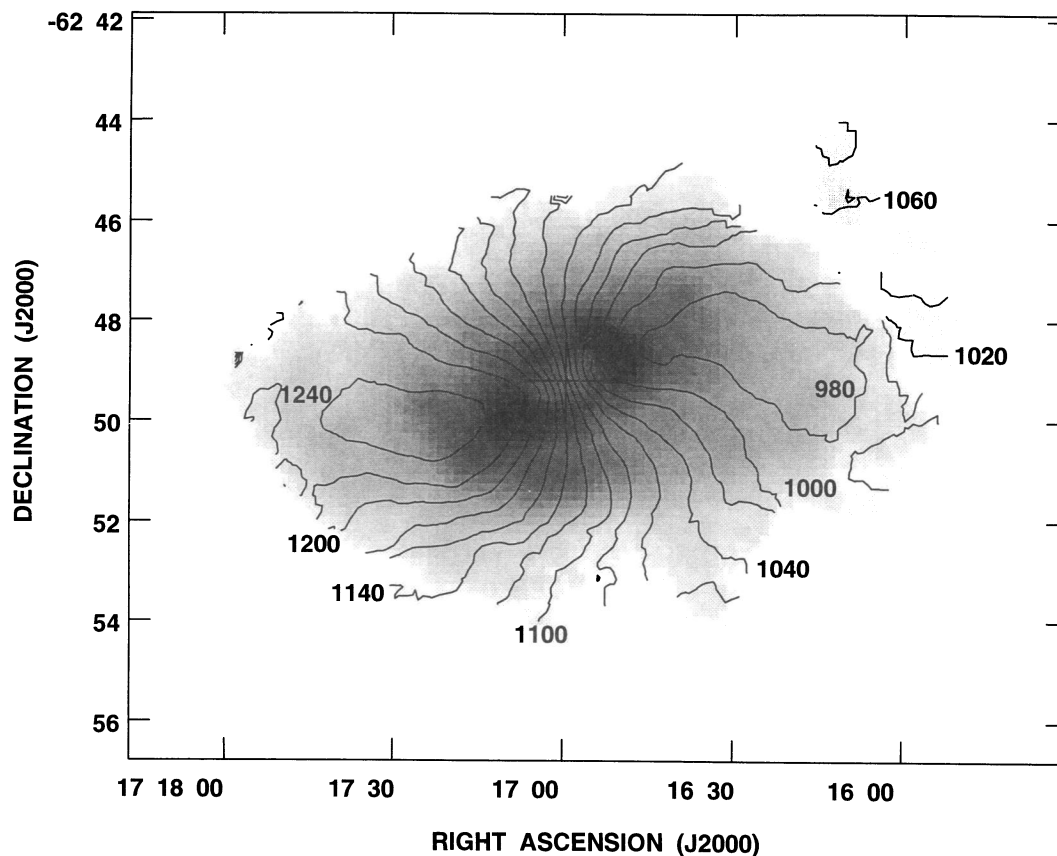


FIG. 15.—Isovelocity contours overlain on the H I column density map of NGC 6300, both formed from a moment analysis of the natural-weighted uv data set. The contour interval is 20 km s^{-1} , and some major velocity contours are marked. The cross marks the position of the dynamical center.

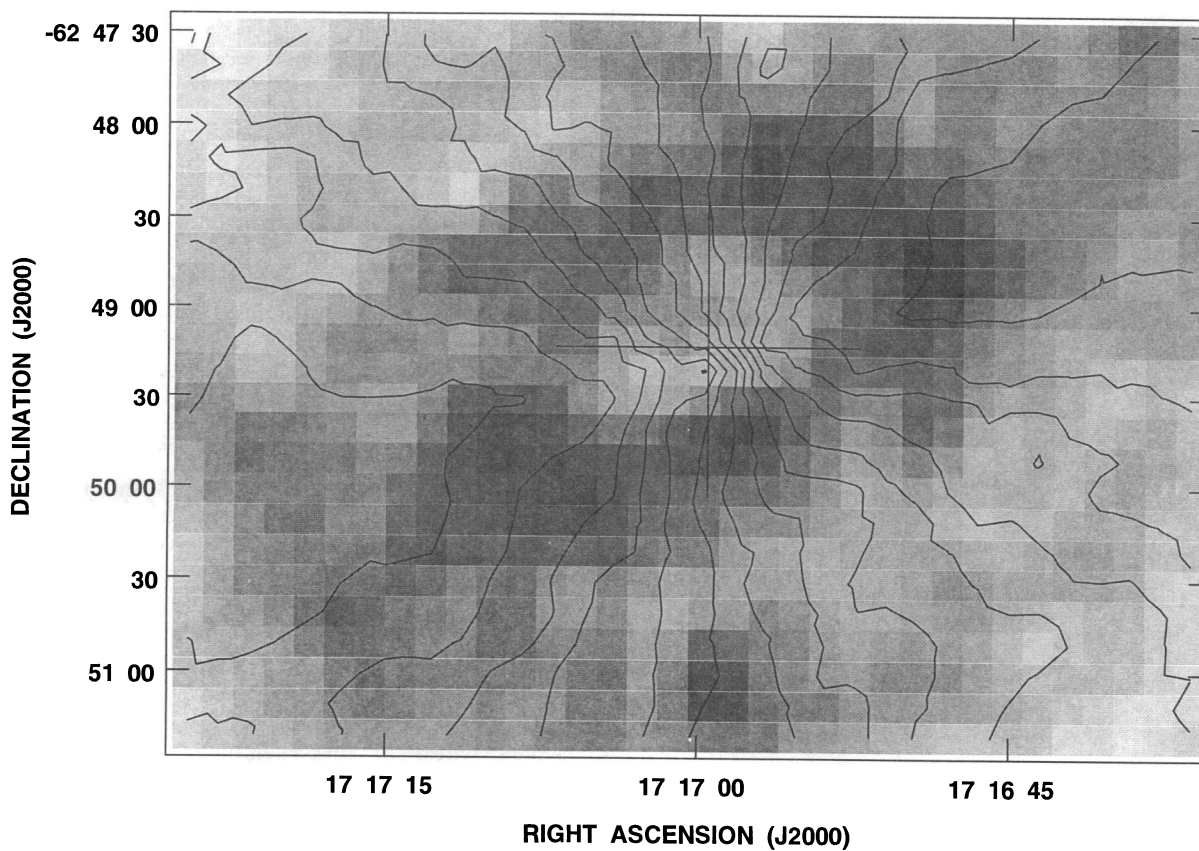


FIG. 16.—Close-up of isovelocity contours in the bar and inner ring region of NGC 6300 overlain on an H I column density map, both formed from a moment analysis of the uniform-weighted uv data set. The contour interval is 20 km s^{-1} , and the cross marks the position of the dynamical center.

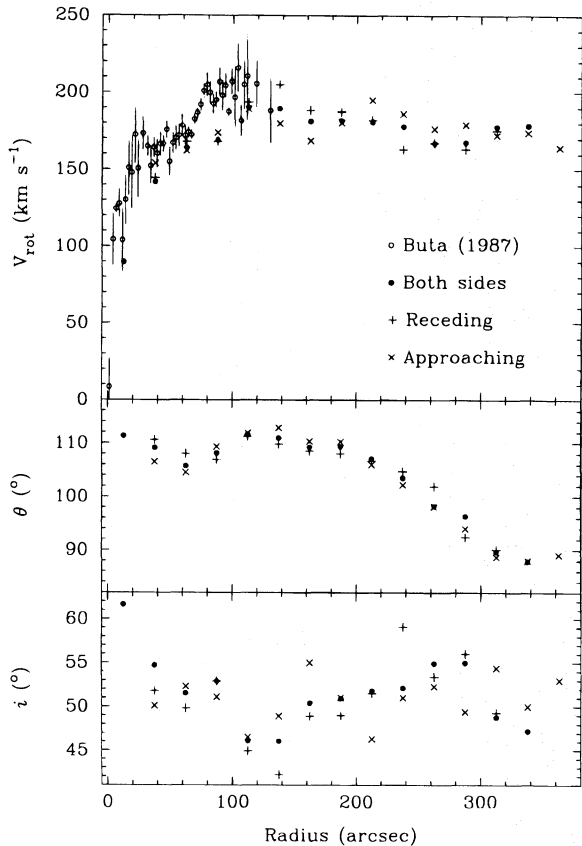


FIG. 17.—Kinematical analysis results for the uniform-weighted velocity field, assuming circular motion in rings inclined at angle i , having line of nodes position angle θ , and with rotation center and systemic velocity fixed. The points are plotted at 1 beamwidth intervals, based on separate fits to the receding (i.e., mostly the eastern) half, the approaching (western) half, and to the entire disk. The open circles in the rotational velocity plot are the optical ionized gas rotational velocities computed by Buta (1987), with fixed $\theta = 108^\circ$ and $i = 52^\circ$.

and [N II]), taken from Table 11 of B87. Some disagreement between the optical and H I rotation curves is to be expected in the inner $40''$ or so, because of the smearing of the steep central velocity gradient by our $25''$ beam, and indeed, the first few H I points do fall slightly below the curve of B87. However, the sudden rise in the optical rotation curve, starting at $r = 60''$ and coinciding with a hump in the light profile due to the inner ring, is not echoed by the H I curve until $r > 80''$. Even then, much of this rise can be attributed to the jump to a lower inclination (and a corresponding increase in the deprojection factor), while the optical rotation curve employs a constant inclination ($i = 52^\circ$) and line of nodes position angle ($\theta = 108^\circ$) throughout. The optical and H I rotation curves are in much better agreement again by the time the optical data run out at $r \sim 130''$. The cause of the disagreement of optical and H I rotation curves near $r = 75''$ is still not clear, but comparisons with the individual optical rotation profiles of NGC 6300 along various position angles (see Table 5 of B87) suggest that noncircular motions associated with the massive arms constituting the inner ring are partly causing the “bump” in the optical rotation curve. It is also important to note that the optical rotation curve is based principally on spectra in four position angles, and that one position angle, 132° , had three separate spectra that carried much of the weight in the solution. As with NGC 1433, a

full survey of the ionized gas velocity field with a Fabry-Perot interferometer may be warranted for a better comparison.

Despite some disagreement between the receding and approaching halves of the velocity field on the actual disk inclination at each radius, there is remarkably good agreement on the kinematic major axis. Once the edge of the optical disk has been reached, the line of nodes slowly but steadily twists some 20° clockwise, from the photometric major axis position angle of 108° to a final position lying due east on the sky. Such warps do not appear to be a common feature in early- to intermediate-type galaxies (Bosma 1991); nevertheless, NGC 6300 still conforms to the first of Briggs’s (1990) empirical “rules” of behavior for galactic warps, in that the onset of the warp occurs between R_{25} and $R_{26.5}$. At the same time, the disk inclination increases steadily from 46° to 55° before dropping back below 50° in the outermost regions (note that there is insufficient gas in the uniform-weighted map at the radial distance of the H I tail to extend the kinematic analysis out that far). The rotation curve of the extended H I disk falls slowly from its peak of 190 km s^{-1} to just below 170 km s^{-1} , before picking up again beyond $r = 300''$ as i is decreased. Although the V-band light distribution of B87 did a surprisingly good job of reproducing the optical rotation curve with just a single value for the mass-to-light ratio, there is clearly still a need for a dark matter halo component to sustain the high H I rotational velocities well outside the optical disk.

3.2.3. Radio Continuum

Figure 18 shows a 600 s continuum-subtracted H α image of NGC 6300 obtained in the same way as described in § 3.1.3, on which has been overlain contours of the (uniform-weighted) 1.38 GHz continuum emission. As expected for a type 2 Seyfert galaxy, there is significant emission from the unresolved nuclear source (coincident with the optical and the dynamical center), amounting to some 15 mJy. Surprisingly, the integrated emission from the galaxy as a whole totals approximately 110 mJy, meaning that the disk component contributes fully 90% of the total flux at 1.38 GHz. This is unusually large for an SBb type galaxy but is not unlike the ratio observed in the ringed SAab galaxy NGC 4736 (Mulder & van Driel 1993). This marks another major difference between NGC 6300 and NGC 1433, which shows a more typical ratio of nuclear to total flux density for Sa and Sab galaxies of 0.32.

Within the resolution (indicated by several point sources in the same field as Fig. 18), the morphology of the extended continuum emission matches quite well that of the star-forming ring, with peaks on the ring major axis, nearly perpendicular to the bar axis. The two extensions on the southern edge have counterparts in the natural-weighted H I map (Fig. 12), only much further out, and indeed, closer examination suggests that these features seen in both maps are in fact low-level artifacts due to the residual effects of a confusing source just outside the primary beam. It may yet be possible to use the four background sources shown in Figure 18, and some even brighter sources further out, to self-calibrate the uv data set, and/or for H I absorption measurements, from which a gas spin temperature in the outskirts of the H I disk could be determined.

The extended nature of the continuum emission in NGC

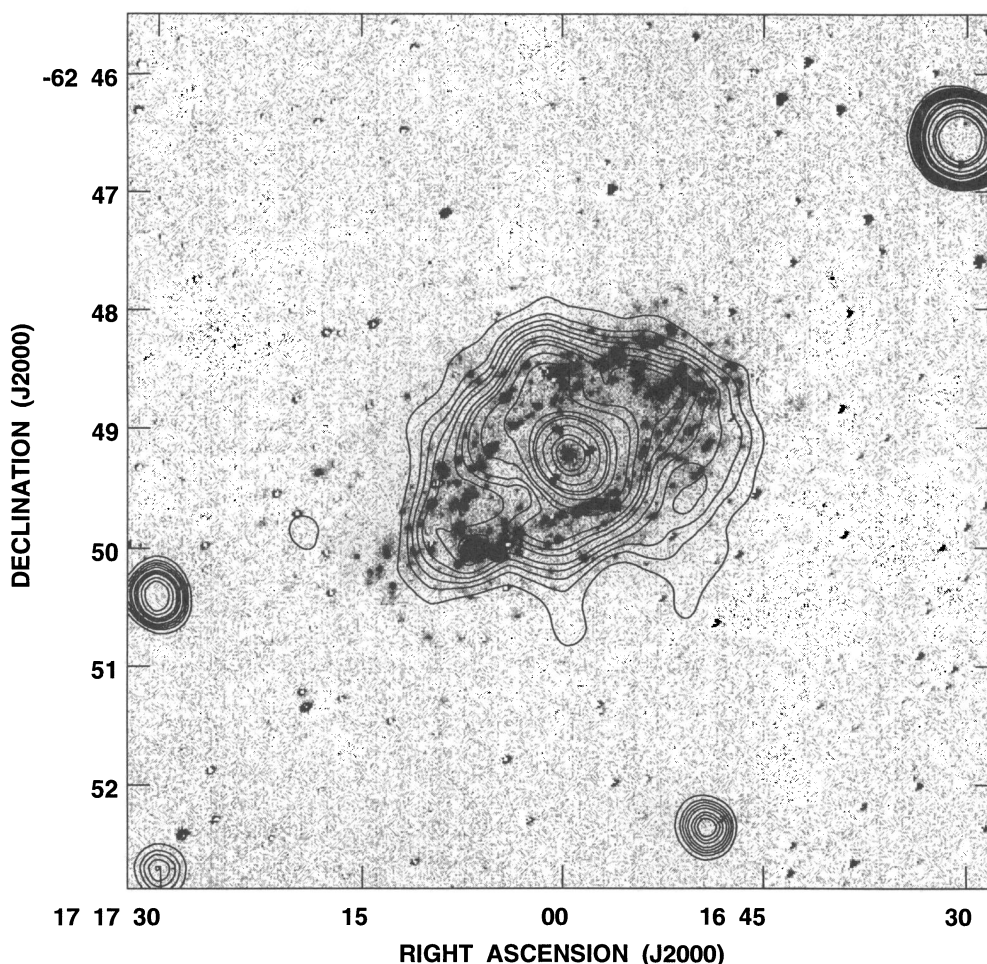


FIG. 18.—Contours of 1.38 GHz continuum flux density overlain on a 600 s continuum-subtracted $H\alpha$ image obtained by D. Crocker and G. Purcell with the CTIO 1.5 m telescope. The radio continuum contours are at levels of 1.0, 1.3, 1.5, 1.7, 1.9, 2.2, 2.4, 2.6, 3.0, 3.4, 4.5, 5.4, 6.0, 8.0, 11.0, 12.5, and 15.0 mJy beam^{-1} . The two extensions to the south are artifacts and should be ignored. The four distinct objects around the edge of this image have flux densities (going clockwise from top right) of 28, 3.3, 2.5, and 4.7 mJy .

6300 requires that we consider the possibility that the H I ring seen in NGC 6300 is purely an absorption effect, rather than an actual deficiency of H I. A comparison of Figures 13 and 18 (both of which are at the same image scale) shows that the H I ring and the extended continuum disk are coextensive, but there is no obvious correlation (or anticorrelation) of H I column density with continuum flux density. The central source is only marginally resolved, if at all, by our $25'' \times 23''$ beam, and yet the central H I hole spans $\sim 2'$ and has an aspect ratio remarkably similar to that of the gas disk as a whole. Thus, while the magnitude of the central H I depression may be exaggerated slightly by the presence of the nuclear continuum source, we are satisfied that the inner H I gas in NGC 6300 does in fact form a nearly closed and continuous ring.

4. DISCUSSION

4.1. The Inclination of NGC 1433

In his study, B86 was unable to assign a definitive inclination for the disk of NGC 1433, since the outermost optical isophotes (usually assumed to be circular in the plane of the galaxy) are influenced by the presence of the outer pseudoring, while statistical studies for a virtually complete sample of southern ringed galaxies (CSRG) indicate that the average outer pseudoring in SB galaxies (though not neces-

sarily *this* particular pseudoring) has an intrinsic axial ratio $q = 0.82 \pm 0.07$. In the former case (ring intrinsically circular), an inclination of 33° follows, but in the latter case (ring axial ratio of 0.85, and assuming the ring major axis to be oriented perpendicular to the bar), the inclination will be closer to 20° . In this section, we aim to demonstrate that, statistics aside, the higher inclination is the only plausible one.

We start by establishing a distance to NGC 1433. Tully (1988) proposes a distance of 11.6 Mpc, based on a redshift consistent with ours, a Hubble constant of $75 \text{ km s}^{-1} \text{ Mpc}^{-1}$, and a Virgocentric infall model. This distance receives some support from a variety of avenues. NGC 1433 is included as a member of the extensive Southern Group Number 13 (Maia, da Costa, & Latham 1989), many of whose other members are also believed to have distances on the order of 12 Mpc. Semi-independent confirmation also comes from the H II region luminosity function (Crocker et al. 1996) which, for an assumed distance of 11.6 Mpc, indicates that the brightest H II regions would have a maximum $H\alpha$ luminosity of just under $10^{39} \text{ ergs s}^{-1}$. This is consistent with an apparent upper cutoff in H II region luminosity of $\sim 10^{39} \text{ ergs s}^{-1}$ noted by Kennicutt, Edgar, & Hodge (1989) in galaxies of type Sb and earlier.

We now apply the Tully-Fisher relation between depro-

jected H I line width W_R^i and absolute blue magnitude $M_B^{b,i}$ as given for field galaxies by Pierce & Tully (1992):

$$M_B^{b,i} = -7.48(\log W_R^i - 2.50) - 19.55 \pm 0.14. \quad (1)$$

Using the corrections prescribed by Tully & Fouqué (1985) for turbulent motion and profile shape, our $W_{20} = 190 \pm 10$ km s⁻¹ equates to a true velocity width $W_R = 155 \pm 9$ km s⁻¹. When deprojected, this becomes $W_R^{i=20} = 453 \pm 26$ km s⁻¹ or $W_R^{i=33} = 285 \pm 17$ km s⁻¹, from which equation (1) predicts $M_B^{b,i=20} = -20.71 \pm 0.33$ and $M_B^{b,i=33} = -19.21 \pm 0.33$. The apparent blue magnitude of NGC 1433, corrected for internal (Tully & Fouqué 1985) and Galactic extinction, is also a function of inclination: $B_T^{i=20} = 10.68 \pm 0.04$ and $B_T^{i=33} = 10.65 \pm 0.04$. Consequently, the distances derived for the two inclination limits differ by a factor of 2; $R(i = 20^\circ) = 19.1 \pm 3.5$ Mpc, while $R(i = 33^\circ) = 9.4 \pm 1.7$ Mpc. For the reasons discussed above, we therefore favor a mean inclination for the disk of NGC 1433 closer to 30° than to 20°. As a consequence, the outer pseudoring of NGC 1433 is, in fact, almost circular in the plane of the galaxy. While it may seem odd that the prototypical ringed barred galaxy would have an intrinsic outer pseudoring axial ratio so much greater than the average, we note that the models of Schwarz (1981) do predict that the stronger bar cases will produce more nearly circular outer rings.

One potential complication that may invalidate this argument is the extent to which noncircular gas motions may disrupt the relationship between luminosity and maximum rotational velocity in a spiral galaxy (Jacoby et al. 1992). As a comparison of Figures 6 and 8 shows, the maximum rotational velocity in NGC 1433 is reached well inside the bar and does not drop much below this maximum, even in regions far from resonance. The maximum residuals between the observed velocity field and a model velocity field with an inclination held fixed at 33° are still no more than 20 km s⁻¹. For a disk inclined at 20° with noncircular motions to emulate a 33° inclination disk in pure circular motion, our kinematical analysis would need to be biased toward inferring unusually high velocities.

From the crowding of gas and stars around the inner ring major axis, it is apparent that particles spend much of their time there by orbiting slower, and therefore they must speed across the ring minor axis to compensate. Since the ROTCUR analysis excludes points within $\pm 25^\circ$ of the kinematic minor axis, which is almost perpendicular to the apparent major axis of the inner ring, we could indeed be favoring unduly large rotation velocities. However, the situation is reversed in the outer pseudoring, and yet the rotational velocity is observed to be only ~ 20 km s⁻¹ lower there than near the inner ring. Thus, we conclude that noncircular motions, while not an insignificant factor, do not corrupt the Tully-Fisher relation to the extent of making the disk appear some 10° closer to face-on than it really is. Still, it is important to note that the Pierce & Tully calibration in equation (1) is based on galaxies having inclinations $i \geq 45^\circ$ and that applying it to galaxies of much lower inclination involves, in a sense, an uncertain extrapolation.

Although the outer pseudoring of NGC 1433 may be more circular than the average outer ring or pseudoring feature in barred galaxies, the inner pseudoring of the galaxy is intrinsically *much more* elongated than the average inner ring or pseudoring feature. For $i = 33^\circ$, the intrinsic axis ratio of the inner pseudoring of NGC 1433 is 0.61

(B86), compared to an average of 0.81 ± 0.06 obtained from the analysis of CSRG data. Thus, NGC 1433 demonstrates how much an individual object can depart from the averages obtained in the CSRG.

4.2. Testing the Resonance Ring Theory

4.2.1. NGC 1433

One of the primary motivations for this study is to use a knowledge of the resonance orbit locations, coupled with the rotation curves, to get a direct measure of the bar pattern speeds in NGC 1433 and NGC 6300. The bar pattern speed is clearly of great importance, since theory predicts that it plays a key role in dictating not only the positions of the resonances, but also how many and what types of resonances will be present (Schwarz 1984; Byrd et al. 1994, hereafter BRSBC). Bar pattern speeds have been estimated in the past (B86; van Driel et al. 1988; van Driel & Buta 1991; Moore & Gottesman 1995; JvM) for a few spiral galaxies, but nearly always, assumptions have had to be made about the shape of the rotation curve, or the location of corotation. As the summary in Table 3 shows, bar pattern speeds measured so far in such galaxies range between approximately 20 and 50 km s⁻¹.

With the information gathered in this study, and from previous photometric analyses (B86; B87), we are now in a position to bypass such assumptions and use the theory of resonance ring formation to measure the bar pattern speed Ω_p directly. In the case of a weak bar, the epicyclic frequency κ is given by linear perturbation theory as

$$\kappa = \left(R \frac{d\Omega^2}{dR} + 4\Omega^2 \right)^{1/2} \quad (2)$$

(e.g., Binney & Tremaine 1987). In the absence of noncircular motions, $\Omega = V/R$, so that

$$\kappa = \sqrt{2} \frac{V}{R} \left(1 + \frac{R}{V} \frac{dV}{dR} \right)^{1/2}. \quad (3)$$

Using the rotation curve in Figure 8, we have plotted the radial variation of the angular frequency Ω , as well as the Lindblad precession frequencies $\Omega + \kappa/2$, $\Omega - \kappa/2$, and $\Omega - \kappa/4$ in Figure 19 [we have taken (dV/dR) to be the average of the slope to either side of each point on the rotation curve]. If the (linear) theory of resonance rings is correct, then each of the resonance curves ought to intersect the vertical line marking the radius of their associated ring

TABLE 3
BAR PATTERN SPEEDS

Galaxy	$ \Omega_p $ (km s ⁻¹ kpc ⁻¹)	Reference
NGC 1365	21 ± 1	Jörsäter & van Moorsel 1995
NGC 1398	48 ± 15 ^a	Moore & Gottesman 1995
NGC 1433	28 ± 7 ^b	Buta 1986
	26 ± 5 ^b	This study
NGC 5101	19	van Driel et al. 1988
NGC 6217	41 ± 3	van Driel & Buta 1991
NGC 6300	27 ± 8 ^c	This study

^a Based on a distance of 16.1 Mpc (Tully 1988), and the uncertainty in associating the ring with a particular resonance.

^b Based on a distance of 11.6 Mpc (Tully 1988).

^c Assuming the inner ring in NGC 6300 corresponds to the $\Omega - \kappa/4$ resonance.

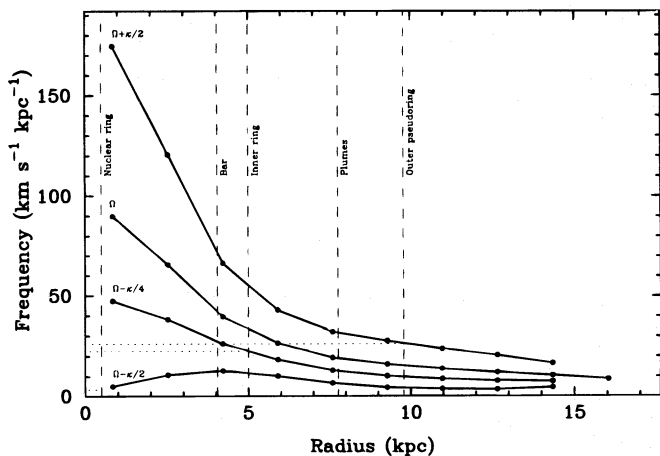


FIG. 19.—The various precession frequency curves for NGC 1433 are shown as solid lines, with their respective frequencies marked. The vertical dashed lines indicate the mean radii of the bar, plumes, and rings, as in Fig. 6, and the horizontal dotted lines mark the bar pattern speed implied if the rings do correspond to specific resonances.

at the same frequency value, namely the bar pattern speed. Based on the mean ring radii determined by B86, we derive $\Omega_p = 3 \pm 1$, 22.4 ± 0.4 , and 26.2 ± 0.4 $\text{km s}^{-1} \text{kpc}^{-1}$ from the nuclear ring, the inner ring, and the outer ring, respectively.

The nuclear ring value is based on an inward extrapolation of the $\Omega - \kappa/2$ curve, and clearly, the effects of beam smoothing in a region with such a steep velocity gradient make this estimate most unreliable. In addition, the linear theory outlined above for the radial variation of Ω and κ may not be appropriate in the region of a strong bar and any associated gas inflow. Unlike the outer pseudoring, which we have surmised to be almost circular, the true axial ratio of the inner ring, being close to ~ 0.6 , makes it difficult to assign a single characteristic radius for this ring. Thus, we assign more weight to the Ω_p implied by the outer pseudoring, although there is still the likelihood that none of the rings lies *exactly* at a resonance. The current theories, however, stop short of predicting precisely where rings will form relative to the resonant orbit locations.

Bearing all these uncertainties in mind (inclination, ring locations relative to resonances, nonlinear effects, etc.), we therefore conservatively propose a value for the bar pattern speed (at the current epoch) in NGC 1433 of $\Omega_p = 26 \pm 5$ $\text{km s}^{-1} \text{kpc}^{-1}$. This would place corotation at $R \sim 6$ kpc, at about 1.5 bar radii, and just beyond the inner ring. From an orbit analysis of the inner ring kinematics only, B86 came up with virtually the same results by assuming a constant rotation velocity across the ring region, although as Figures 6 and 8 show, this is not strictly the case. We can also now confirm that the gas-deficient regions seen in Figure 4 between the inner and outer H I rings must be related to the vacant “banana” orbits near the L_4 and L_5 points at corotation, as predicted by the strong-bar models of Schwarz (1981) and Contopoulos & Papayannopoulos (1980).

BRBC used test-particle simulations to improve upon the earlier work of Schwarz (1981, 1984) by testing the effects of bar pattern speeds, bar strength, and rotation curve form on the number and location of rings formed in the evolving models. Using a combination of a flat rotation curve (not unlike Fig. 8), a “strong” bar (relative radial force from the bar of 20%), and a “medium to slow” bar

domain pattern speed, they were able to produce after just four bar rotations a gas particle distribution with an uncanny resemblance to our H I map of NGC 1433 (compare our Fig. 4 to the lower right panel of their Fig. 12b), even to the extent of reproducing gas peaks near the “plume” features seen optically. Although Table 3 provides a much too limited sample from which to draw any solid conclusions, it seems not unreasonable that the “slow to medium” domain of bar pattern speed would include our $\Omega_p \sim 26$ km s^{-1} for NGC 1433, with perhaps the “fast” pattern speed domain therefore encompassing values of Ω_p of 50–60 km s^{-1} and upward.

4.2.2. NGC 6300

Having found satisfactory agreement with the theory in the case of NGC 1433, we next turn our attention to NGC 6300. Figure 20 shows the precession frequency curves for NGC 6300, based purely on the optical rotation curve data from B87 for $R < 9.3$ kpc, and on our H I rotation curve thereafter. Owing to the vastly better sampling of points in the inner disk of NGC 6300 compared to NGC 1433, the radius axis has been plotted on a logarithmic scale. The vertical dashed lines here mark not separate rings, but the same approximate boundaries for the broad inner ring, as given by B87 and marked in Figure 14. By again associating this inner ring feature with the inner second harmonic resonance, we would infer a bar pattern speed for NGC 6300 in the broad range $\Omega_p = 27 \pm 8$ km s^{-1} . Thanks to the extended radial coverage from our H I data, we would therefore expect to see some sign of an outer ring or pseudoring somewhere between $R = 8$ –14 kpc, where the Ω_p limits intersect the $\Omega + \kappa/2$ curve. Figure 14 reveals no such feature in this range ($115'' < r < 200''$), the bump at $r = 145''$ already having been ascribed to short spiral segments, and not a complete ring (§ 3.2.1).

In the same vein, these Ω_p limits based on the inner ring also intersect the $\Omega - \kappa/2$ locus at a number of radii. According to the resonance ring theory, there ought therefore to be at least one nuclear ring, probably inside $R = 0.8$

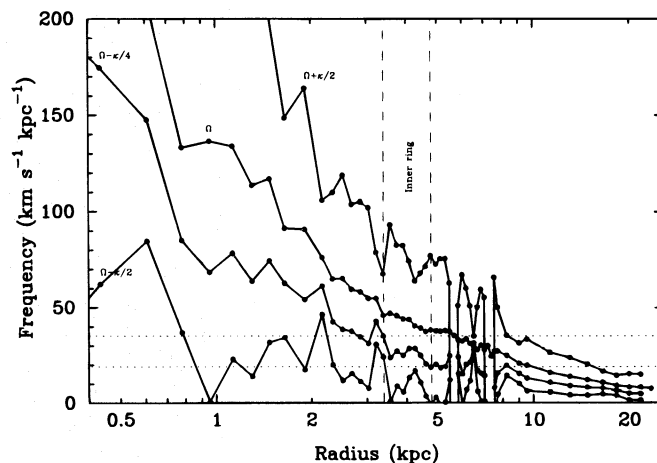


FIG. 20.—The various precession frequency curves for NGC 6300 are shown as solid lines, with their respective frequencies marked. The vertical dashed lines indicate the approximate extent of the inner ring, and the horizontal dotted lines mark the possible bar pattern speed range implied if this ring was in fact associated with the $2HR^-$ resonance. Note that the radius scale is plotted logarithmically to accommodate the different sampling in the optical and H I regimes.

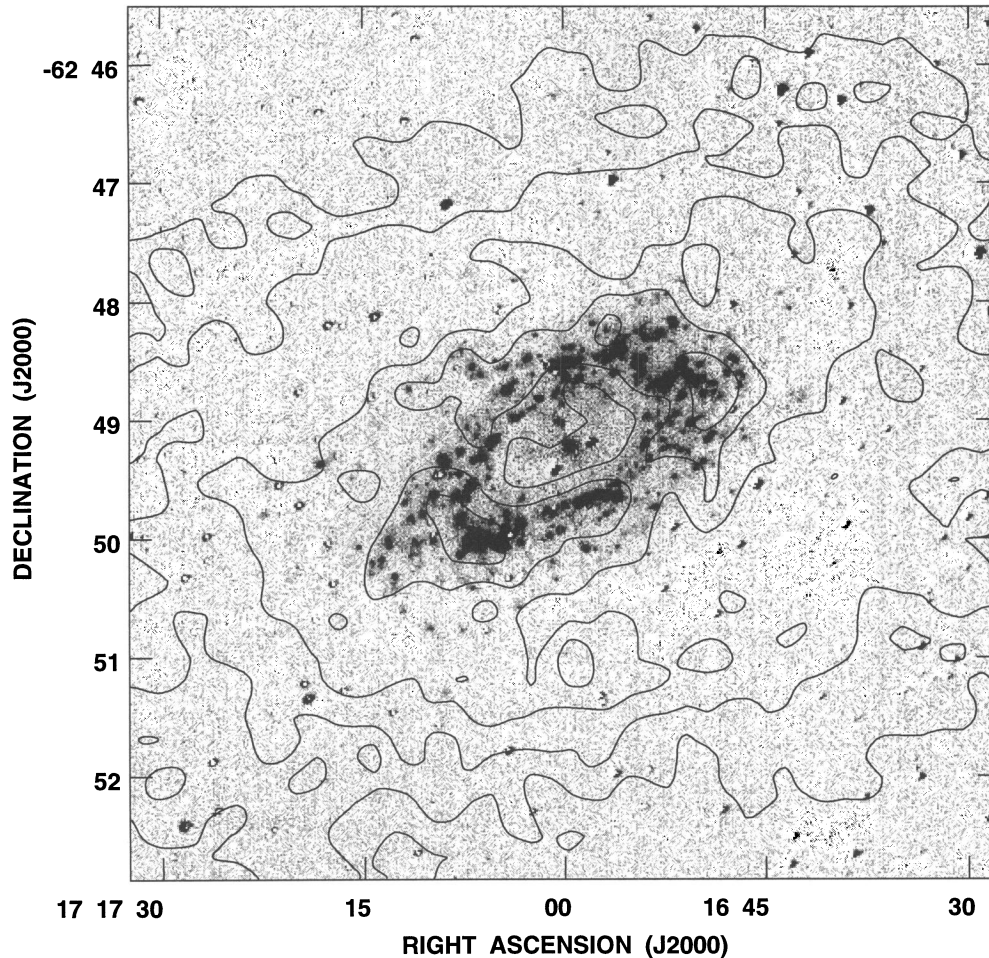


FIG. 21.—Contours of H I column density as shown in Fig. 13 overlain on the same H α image as in Fig. 18. Notice the extremely good agreement between both the gas morphology and column density when compared with the distribution and brightnesses of the H II regions, and with the stellar ring (Fig. 13).

kpc. Such a ring would be no bigger than our synthesized beamwidth and would not be apparent in Figure 14. No optical nuclear ring was reported by B87, although such a ring could conceivably be camouflaged by the foreshortened bar, dust lanes, or the type 2 Seyfert nature of the nucleus (Phillips, Charles, & Baldwin 1983).

Therefore, we are left to conclude that either the resonance ring theory for the origin of stellar and gaseous rings (which performed creditably in the case of NGC 1433) is flawed, or else the ring in NGC 6300 may not be a feature directly driven by the bar. There is reason to believe that the latter situation is a definite possibility. B87 noted that when NGC 6300 is approximately deprojected, the inner pseudoring is aligned neither parallel nor perpendicular to the bar, but at an intermediate angle. Sygnet et al. (1988) have suggested that NGC 6300 is a multiple pattern speed galaxy because of this misalignment. Sellwood & Sparke (1988) have suggested that spiral patterns in barred galaxies may not, in general, be driven by the bar, but are independent patterns with a slower pattern speed than the bar. Tagger et al. (1987), Sygnet et al. (1988), and Sellwood & Sparke (1988) have discussed the idea of mode coupling between the spiral and bar patterns. In this scenario, the corotation radius of the bar coincides with the radius of the inner Lindblad resonance (ILR) of the spiral. As a consequence of the different pattern speeds, one would expect a random distribution of phase difference between the ends of the bar

and the beginning of the spiral arms. In the case of NGC 6300, we note that the spiral structure does not begin at the ends of the bar, but about 30° ahead of the bar. However, Sellwood & Sparke (1988) present simulations showing that even with different pattern speeds, the spiral and the bar will often appear smoothly connected.

It is possible for an inner resonance ring to be composed of distinct segments, like that of NGC 1433, but the H I “spurs” extending from the gas ring of NGC 6300 indicate that the spiral arm segments in NGC 6300 are much less tightly confined than those in NGC 1433. Still another difference between NGC 6300 and NGC 1433 is that the peaks in the H I ring of NGC 6300 do lie along the ring major axis (partly because of projection effects), but this then places them almost perpendicular to the bar axis, rather than along the bar axis as is the case in NGC 1433. Finally, despite apparently having a fast bar powerful enough to drive gas inflows, there are no relatively empty regions near corotation in NGC 6300 analogous to those in NGC 1433.

There is a third possibility, originally outlined by B87, which is that the tightly wound spiral arms in NGC 6300 are still in the process of forming a closed, continuous resonance ring. It takes time for the torques exerted by the bar to stretch spiral features into rings, and continual gas infall or recycling can retard this evolution. The presence of an extended, warped H I disk and gas tail in NGC 6300 may point to ongoing gas accretion in this galaxy. The simula-

tions of BRSBC have shown how two galaxies with nearly the same pattern speed (such as NGC 1433 and NGC 6300) can still appear morphologically quite distinct, if only because one galaxy was slower to develop a bar asymmetry (not to mention the possibility that bars may be destroyed and reformed many times during a Hubble time; Sellwood & Wilkinson 1993).

Further support for the evolution scenario is provided by Figure 21, which shows contours of the uniform-weighted H I surface density on the H α image used in § 3.2.3. When compared with Figure 13, it is clear that the recent massive star formation in NGC 6300 follows the H I ring much better than does the older and slightly smaller stellar pseudoring. Thus, the stellar orbits (which are slower to react to the bar torques than the gaseous component) could be stretched still further in the next few Gyr, although any further slowdown in the bar pattern speed will cause the stellar ring to take even longer to reach its final mature stage. This evolution may also be associated with a transition from a disk-dominated to a (nucleus+bar)-dominated radio continuum source.

Finally, an outer ring will take much longer to form than an inner ring, while the nuclear ring will form quickest of all ($\sim 10^7$ – 10^8 yr; Combes 1993). Thus, if a nuclear ring could be confirmed in NGC 6300, perhaps from near-IR imaging, then the case for interpreting NGC 6300 as a barred spiral evolving into a resonance ring galaxy (with NGC 1433 representing the pinnacle of this evolution) would be strengthened further.

The nearby barred spiral galaxy NGC 1365 possesses an outer pseudoring (CSRG) and shares some of the H I characteristics of both NGC 1433 and NGC 6300. In a recent comprehensive VLA H I study, JvM found that just like in NGC 1433, the H I disk in NGC 1365 does not extend much beyond the optical disk, and there is an almost complete H I ring visible in their low-resolution map at the radial distance of the optical pseudoring. In other ways, however, NGC 1365 has more in common with NGC 6300, such as the presence of a warp and an asymmetric extension to the gas disk. By associating dust-lane arm crossings with corotation, and minima in the streaming motions along the arms with individual resonances, JvM used an analysis not dissimilar to ours to arrive at a bar pattern speed of $\Omega_p = 21 \pm 1 \text{ km s}^{-1}$. However, this would place the outer Lindblad resonance at $R \sim 208''$, barely 2/3 of the radial distance of the optical and H I pseudoring. In addition, despite the obvious presence of a strong bar, the L_4 and L_5 regions have not been evacuated to the same degree as for NGC 1433. Thus, unless NGC 1365 possesses multiple pattern speeds, its status as a bona fide resonance ring galaxy akin to NGC 1433 is still open to question.

5. CONCLUSIONS

In this paper we have presented the distribution and velocity fields of neutral hydrogen in NGC 1433 and NGC 6300, two of the closest ringed barred spirals in the southern sky. Though classified similarly with regard to morphology, the two objects are quite dissimilar in many respects. We summarize our main results for each object separately. For NGC 1433, we have found the following:

1. An H I distribution that follows the optical structure very closely. The inner ring and outer pseudoring are very well defined in the H I map, as well as the two secondary arcs (or “plumes”) off the leading sides of the inner ring.

There is also central emission with a peak slightly to the east of the nucleus. The bar region, and the areas between the inner and outer rings along the bar minor axis line, are deficient in neutral atomic hydrogen.

2. Each ring feature in NGC 1433 is associated with a maximum in the azimuthally averaged gas surface density. The plumes are only local maxima at their radii.

3. If the outer isophotes of NGC 1433 represent an axisymmetric region, then the inclination of the system must be close to 33° . However, if the outer pseudoring is intrinsically oval, as is typically the case, then the inclination could be 20° or less. Application of the Tully-Fisher relation to the H I data favors the higher estimate of the inclination, meaning that in spite of the strong bar, the outer pseudoring of NGC 1433 is nearly circular in the disk plane. On the other hand, this also implies that the inner ring of NGC 1433 is intrinsically much more elongated than the average.

4. The strength of the (nonthermal) radio continuum emission in NGC 1433 is well correlated with the local density of H II regions, with roughly equal contributions coming from each end of the bar and from the nucleus. Although a definite detection is far from certain, we have been able to place an upper limit on the present 1.38 GHz flux density from the Type II SN 1985P as $S_{1.38 \text{ GHz}} < 0.5 \text{ mJy}$.

5. By identifying the outer pseudoring with the outer Lindblad resonance, the H I rotation curve of NGC 1433 gives a bar pattern speed of $26 \pm 5 \text{ km s}^{-1} \text{ kpc}^{-1}$. This pattern speed is consistent with the location of the inner 4:1 resonance being near the position of the inner ring, but our observations lack the spatial resolution to test for an association of the nuclear ring with the inner Lindblad resonance. The gas-deficient regions between the two rings appears to be associated with the Lagrangian points L_4 and L_5 , which are located at corotation along the minor axis line of the bar. The orbits in these regions are unstable in the presence of a strong bar. Thus, the structure of NGC 1433 compares favorably with test particle models of barred spirals.

For NGC 6300 we have found the following:

1. The H I distribution extends well beyond the optical disk. This is very unlike NGC 1433 and highlights a fundamental difference between the two systems. Like NGC 1433, however, the inner pseudoring is a region of gas concentration. There are no deficiencies of gas in the regions outside the inner ring in which the Lagrangian points L_4 and L_5 might be expected to be found.

2. Throughout most of the optical disk, the azimuthally averaged surface density of H I gas in NGC 6300 is higher than in NGC 1433. The maximum surface density is found near the location of the inner pseudoring, and the density peak is broader than the extent of the optical ring.

3. The extended H I disk of NGC 6300 exhibits both a loose “tail” feature on its western edge and a 20° warp in its kinematic line of nodes. The overall H I mass-to-blue luminosity ratio is not, however, unlike that for NGC 1433 or for Sab galaxies in general.

4. We confirm the existence of noncircular gas motions in the bar region, as hinted at by optical emission-line spectroscopy, but such motions seem to be confined within the inner H I ring. There appears to be a discrepancy between the optical rotational velocity curve derived from a series of

spectra at various position angles and the rotation curve derived from the global H I velocity field, which is most apparent in the region of the inner pseudoring.

5. Emission from within the inner ring of NGC 6300 totally dominates even the contribution from the type 2 Seyfert nucleus to the 1.38 GHz continuum.

6. On the assumption that the inner pseudoring in NGC 6300 is associated with the inner 4:1 resonance, we find $\Omega_p = 27 \pm 8 \text{ km s}^{-1} \text{ kpc}^{-1}$. However, there is no trace optically or in the H I of either an outer pseudoring or a nuclear ring at the positions implied if this is indeed the case. While it may be that the inner pseudoring of NGC 6300 has little to do with resonance phenomena at all, we have also presented several arguments for why we believe NGC 6300 may represent merely a “juvenile” stage in the transition from a barred spiral to a fully fledged resonance ring galaxy such as NGC 1433.

Although this study has provided one of the first opportunities to directly compare real examples of resonance ring galaxies with numerical models, there is still much work that needs to be done both observationally and theoretically. As Table 3 attests, the sample of galaxies for which direct measurements of bar pattern speeds are available is still somewhat limited for examining the influence of pattern speed domain on galactic structure. Although the

linear perturbation theory used in this analysis may not be strictly appropriate in the central regions of these galaxies in the presence of noncircular motions, the key limiting factors are still a lack of spatial resolution and no specific predictions of where the gas and stellar rings ought to lie relative to the resonant orbit locations. Even so, many key predictions of the Schwarz (1981) and BRSBC models have been borne out by these new observations, and we may even have the beginnings of an evolutionary sequence for resonance ring galaxies.

We are grateful to D. Crocker and N. Killeen for installing and maintaining the AIPS software at the University of Alabama, and to V. McIntyre for producing Figure 1. We wish to thank G. Purcell, D. Crocker, and M. Mazzolini for supplying data in advance of publication, and we acknowledge useful comments from G. Byrd, B. Koribalski, and an anonymous referee. This research has made use of the NASA/IPAC Extragalactic Database (NED), which is operated by the Jet Propulsion Laboratory, Caltech, under contract with the National Aeronautics and Space Administration. H. T. acknowledges support from CONACYT through a graduate student scholarship and DGAPA/UNAM through grant IN107094. This work has been supported by EPSCoR grant EHR-9108761.

REFERENCES

- Athanassoula, E., Bosma, A., Creze, M., & Schwarz, M. P. 1982, *A&A*, 107, 101
- Barbon, R., Cappellaro, E., & Turatto, M. 1989, *A&AS*, 81, 421
- Begeman, K. 1987, Ph.D. thesis, Univ. Groningen
- Binney, J., & Tremaine, S. 1987, *Galactic Dynamics* (Princeton: Princeton Univ. Press)
- Bland-Hawthorn, J., Taylor, K., Veilleux, S., & Shopbell, P. L. 1994, *ApJ*, 437, L95
- Bosma, A. 1991, in *Warped Disks and Inclined Rings Around Galaxies*, ed. S. Casertano, P. Sackett, & F. Briggs (Cambridge: Cambridge Univ. Press), 181
- Briggs, F. H. 1990, *ApJ*, 352, 15
- Buta, R. 1984, Ph.D. thesis, Univ. Texas At Austin (Univ. Texas Publ. in Astron. 23)
- . 1986a, *ApJS*, 61, 609
- . 1986b, *ApJS*, 61, 631 (B86)
- . 1987, *ApJS*, 64, 383 (B87)
- . 1995, *ApJS*, 96, 39 (CSRG)
- Byrd, G., Rautiainen, P., Salo, H., Buta, R., & Crocker, D. A. 1994, *AJ*, 108, 476 (BRSBC)
- Chevalier, R. A., & Fransson, C. 1994, *ApJ*, 420, 268
- Combes, F. 1993, in *N-Body Problems and Gravitational Dynamics*, ed. F. Combes & E. Athanassoula (Paris: Observatoire de Paris), 137
- Condon, J. J. 1992, *ARA&A*, 30, 575
- Contopoulos, G. 1979, in *Photometry, Kinematics, and Dynamics of Galaxies*, ed. D. Evans (Austin: Univ. Texas Press), 425
- Contopoulos, G., & Papayannopoulos, T. 1980, *A&A*, 92, 33
- Crocker, D., Baugus, P., & Buta, R. 1996, in preparation
- de Vaucouleurs, G. 1963, *ApJS*, 8, 31
- de Vaucouleurs, G., de Vaucouleurs, A., Corwin, H. G., Buta, R. J., Paturel, G., & Fouqué, P. 1991, *Third Reference Catalogue of Bright Galaxies* (New York: Springer) (RC3)
- Higdon, J., & Buta, R. 1996, in *IAU Colloq. 157, Barred Galaxies*, ed. R. Buta, B. Elmegreen, & D. Crocker, in press
- Jacoby, G. H., et al. 1992, *PASP*, 104, 599
- Jörsäter, S., & van Moorsel, G. A. 1995, *AJ*, 110, 2037 (JvM)
- Kennicutt, R. C., Edgar, B. K., & Hodge, P. W. 1989, *ApJ*, 337, 761
- Kormendy, J. 1979, *ApJ*, 227, 714
- . 1982, in *Morphology and Dynamics of Galaxies*, ed. L. Martinet & M. Mayor (Sauverny: Geneva Obs.), 115
- Maia, M. A. G., da Costa, L. N., & Latham, D. W. 1989, *ApJS*, 69, 809
- Mazzolini, M., et al. 1996, in preparation
- Moore, E. M., & Gottesman, S. T. 1995, *ApJ*, 447, 159
- Mulder, P. S., & van Driel, W. 1993, *A&A*, 272, 63
- Phillips, M. M., Charles, P. A., & Baldwin, J. A. 1983, *ApJ*, 266, 485
- Pierce, M. J., & Tully, R. B. 1992, *ApJ*, 387, 47
- Reif, K., Mebold, U., Goss, W. M., van Woerden, H., & Siegman, B. 1982, *A&AS*, 50, 451
- Reynolds, J. 1994, private communication
- Roberts, M. S., & Haynes, M. P. 1994, *ARA&A*, 32, 115
- Rupen, M. P., van Gorkom, J. H., Knapp, G. R., Gunn, J. E., & Schneider, D. P. 1987, *AJ*, 94, 61
- Ryder, S. D., Staveley-Smith, L., Dopita, M. A., Petre, R., Colbert, E., Malin, D. F., & Schlegel, E. 1993, *ApJ*, 416, 167
- Ryder, S. D., Staveley-Smith, L., Malin, D., & Walsh, W. 1995, *AJ*, 109, 1592
- Schwarz, M. P. 1981, *ApJ*, 247, 77
- . 1984, *MNRAS*, 209, 93
- Sellwood, J. A., & Sparke, L. S. 1988, *MNRAS*, 231, 25
- Sellwood, J. A., & Wilkinson, A. 1993, *Rep. Prog. Phys.*, 56, 173
- Syget, J. F., Tagger, M., Athanassoula, E., & Pellat, R. 1988, *MNRAS*, 232, 733
- Tagger, M., Syget, J. F., Athanassoula, E., & Pellat, R. 1987, *ApJ*, 318, 43
- Tully, R. B. 1988, *Nearby Galaxies Catalogue* (Cambridge: Cambridge Univ. Press)
- Tully, R. B., & Fouqué, P. 1985, *ApJS*, 58, 67
- van Driel, W., & Buta, R. J. 1991, *A&A*, 245, 7
- van Driel, W., Rots, A. H., & van Woerden, H. 1988, *A&A*, 204, 39
- Warmels, R. H. 1986, Ph.D. thesis, Univ. Groningen
- Weiler, K. W., Van Dyk, S. D., Sramek, R. A., & Panagia, N. 1995, in *IAU Colloq. 145, Supernovae & Supernova Remnants*, ed. Z. Wang & R. McCray, in press
- Wevers, B. M. H. R. 1984, Ph.D. thesis, Univ. Groningen